Design of resonant structures in resin matrix to mitigate the blast wave with a very wide frequency range

Q.Q. Li[a*], Z.C. He[b], E. Li[c*], P. Liu[a], X.Y. Lin[b], Y. Wu[b]

[a] *College of Automotive and Mechanical Engineering, Changsha University of Science and Technology, 410114, Yuhua District, Changsha City, Hunan Province, P. R. China*

[b] *State Key Laboratory of Advanced Design and Manufacturing for Vehicle Body, Hunan University, Changsha, 410082 P. R. China*

[c] *School of Science, Engineering & Design, Teesside University, Middlesbrough, UK*

Abstract

In this work, resonant structures (RSs) are embedded in the resin matrix to form the micro-scale artificial composite materials to mitigate the blast wave with a very wide frequency range (BWR). The propagation of stress waves in the resin and composite materials is described, and the composite materials exhibit stronger blast wave attenuation characteristic compared with the pure resin material. The attenuation mechanism of the composite materials is explained in detail through the absorption, storage and conversion of impact energy. In addition, the influences of materials of the RSs on the performances of the composite materials are analyzed, and the RS is redesigned to further improve the attenuation effect of the composite material. Equivalent model of the composite material is first proposed and established based on the weakly nonlinear lattice system (WNLS). At the same time, artificial tree (AT) algorithm is applied to design its spring stiffness parameters. Based on the WNLS, a three-dimensional composite material plate structure is built to mitigate the overpressure of blast wave at the macro-scale. Compared with traditional materials, the composite material exhibits superior attenuation effect and greater lightweight.

***Key words*:** composite material, micro- and macro- scale, resonant structures; blast wave with a very wide frequency range; weakly nonlinear lattice system;

*Corresponding author.
E-mail address: hdliqiqi@163.com (Q.Q. Li)
E-mail address: q.li@tees.ac.uk (E. Li)

1 Introduction

Blast wave generated by explosion causes great damage to the human body [1, 2]. Therefore, it is very significant to study to effectively reduce the overpressure of blast wave in order to protect the human body. Previous scholars have studied ways to use different forms of material and structure [3-7] to mitigate blast waves. Nesterenko [8] studied the attenuation effect of the "soft" condensed matter by using a simplified approach, and some anomalous effects were also analyzed. Christou et al. [9] presented a computational continuum model of fluid–structure interaction to study the mitigation effects of foam structure, foam structure with filler SiO_2 aerogel and foam structure with filler soda-lime glass beads, respectively. Wadley et al. [10] proposed the concept of cellular materials to achieve active and passive attenuation of blast wave overpressure. Through pre-compress the cellular material and release prior to the arrival of the explosion blast wave, a momentum opposite to the explosion was produced. It can achieve the offset of the momentum of the blast wave. Su et al. [11] studied one novel device consisting of a piston-cylinder to mitigate the blast wave. When the device is subjected to the blast wave, the blast wave is generated inside and repeatedly reflected. Numerical simulations show that the device can significantly reduce the peak pressure of the blast wave. Vivek and Sitharam [12] used a proportional test equipment to study the attenuation effect of a sealed sand barrier system on the blast wave. The test results show that the sand barrier system can effectively attenuate the shock wave, and the geotextile layer plays an important role in providing a gradual upward pressure on the downstream end of the barrier. Dan and Ozer [13] studied the propagation characteristics of blast waves through a set of plate barriers. Numerical results show that these plate barriers can effectively mitigate the blast wave.

In short, studies on blast wave protection mainly focuses on using material deformation to absorb blast wave energy, using complex structure to alleviate blast wave propagation or using the inverse potential energy principle to counter incoming

blast wave. These measures require large material damage or complex and large structure which mean these measures cannot be reused or require a large volume and cost. Fortunately, scholars have used RSs to overcome the shortcomings of these traditional methods. RS can be reused many times and can efficiently attenuate blast waves with a small and lightweight structure [14, 15]. RSs exhibit extraordinary physical properties [16-21] through the local resonance of oscillators, and these physical properties can effectively attenuate the blast wave.

Li et al. [14] proposed a multi-resonator RS. Theory studies demonstrate that the multi-resonator RS has more band gaps compared with traditional RSs. Numerical results prove that the multi-resonator RS can achieve a great attenuation effect of blast wave. In addition, sensitivity analyses give effects of parameters of the RS on blast wave attenuation. Tang et al. [15] applied the negative effective mass property of RSs to mitigate the impact load and blast wave. The influences of number and mass of resonator on the frequency spectrum and amplitude were also studied. Wang et al. [22] proposed a novel method to study the attenuation effect of polymer matrix with particles on blast wave. The three-dimensional models of two kinds of RSs were set up, and the energy absorption and particle motion were studied. Mitchell et al. [23, 24] designed the metaconcrete to attenuate the elastic waves. The resonant motions of inclusions can significantly absorb the impact energy and reduce the structure stress. Sagr et al. [16] presented a dissipative RS with multiple Maxwell oscillators. The vibration and dissipation characteristics were studied by the damped single-resonator and dual-resonator microstructure models. The dissipative RS was applied to mitigate the blast wave. The band gaps of blast wave were expanded significantly by reasonably designing the resonant motions and viscoelastic damping effects of oscillators [25, 26]. Although scholars have conducted studies on blast wave protection based on RSs, few works have mentioned the design of dual-scale RSs for the attenuation of BWR. The attenuation of BWR involves two key factors. The first one is how to design the RS to enhance their attenuation effects. The second factor is how to achieve macro-scale verification after completing the micro-scale design of RSs.

Resin material is a kind of common engineering material, which has the edges of

light weight, low cost, and easy manufacturing. In addition, resin materials are a good choice for the matrix of composite materials although the mechanical and physical properties of pure resin are not outstanding. Composite materials produced by the resin matrix and other high-performance filler materials can bring a leap in material properties. For example, the composite material of carbon fiber and resin matrix is characterized with high strength and light weight [27, 28], the composite material of waste paper/jute fabric and resin matrix has high mechanical performance and environmental protection property [29], and the combination of graphene sheet and resin matrix can make paints own extremely strong conductive property [30].

Starting from the design difficulties of RSs and the excellent properties of resin, we embed the RSs into the resin matrix to form a new composite material at the micro-scale. The new composite material has excellent mechanical and physical properties, which can effectively alleviate the BWR and absorb the impact energy. Sensitivity analyses of materials of the RSs are carried out to enhance the attenuation effect of composite material, and the RS is redesigned to further improve the performance of the composite material. In addition, the energy absorption characteristics of the composite materials are presented to explain the attenuation mechanism of blast waves. Furthermore, an equivalent model is set up based on the WNLS to model the performance of the composite material. Finally, a macro-scale composite material plate structure is built based on the equivalent model to attenuate the blast wave overpressure and verify the attenuation effect of RSs.

This work is organized as follows. In Section 2, the micro-scale composite material model with internal RSs is established, and sensitivity analyses of the materials and studies on an improved RS model are presented. Section 3 describes the theory of the WNLS and the inverse of spring stiffness parameters. The attenuation effects of the macro-scale composite material model are studied in Section 4. A preliminary experimental scheme is provided in Section 5. Finally, Section 6 gives the conclusions.

2 Blast wave mitigation with the micro-scale composite material

2.1 Model of composite material with RSs

Resin is a common material in engineering, with the advantages of low price and mature technology. In this work, a micro-scale composite material structure consists of RSs and resin matrix is applied to study the propagation characteristics of stress waves. Fig. 1 shows the composite material model which length, width, and height are 2 mm, 1 mm, and 1 mm, respectively. The RSs that are embedded in the resin matrix consist of frame, coating and oscillator. Seven layer resin materials and six layer RSs are periodically arranged in the entire structure. The cylindrical holes are periodically arranged on the frame structure, and the coating and oscillator structures are installed in these holes. Fig. 2 shows the detailed size of one RS. Oscillator is a cylindrical structure, and its thickness and circular diameter are 60 μm and 100 μm. The wall thickness of the coating structure is 10 μm. The materials of frame, coating and oscillator are PP resin, PP resin and steel. Table 3 shows the parameters of these two materials.

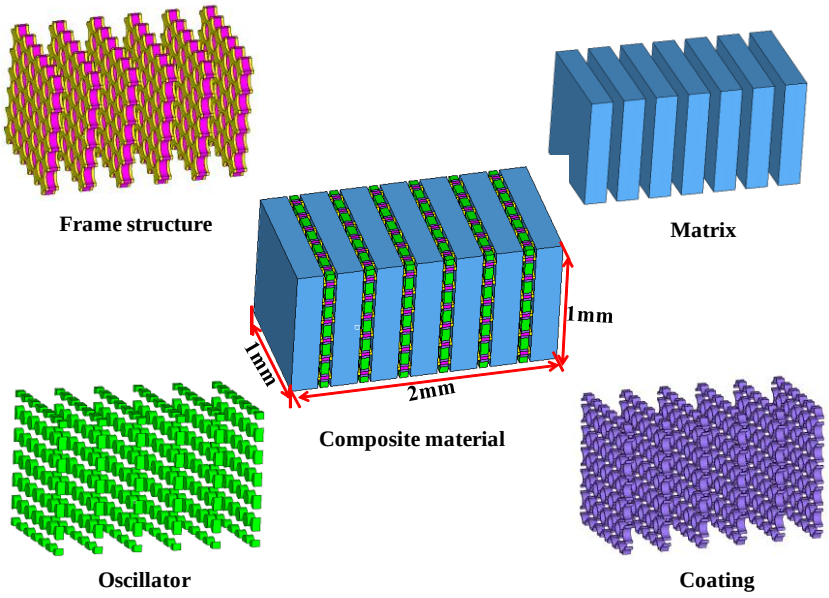

Fig. 1. Composite material with internal RSs.

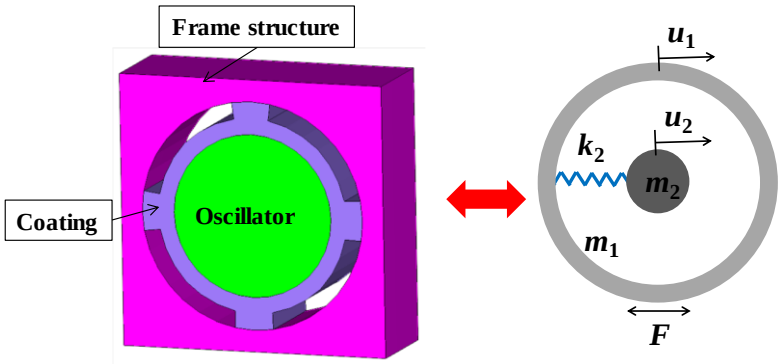

(a) One RS

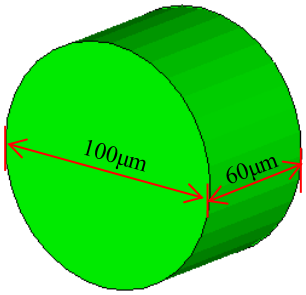

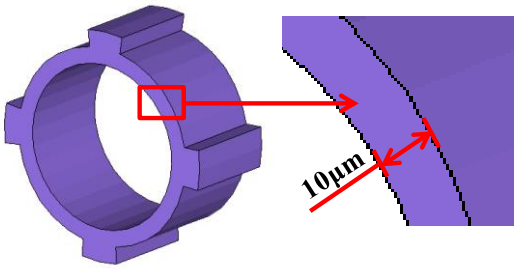

(b) Detailed size of one oscillator (c) The coating structure

Fig. 2. Details of one RS.

2.1.1 Model analysis of the single-resonator microstructure

As shown in Fig. 2 (a), the RS in the composite material can be equivalently viewed as the single-resonator microstructure. Its outer and inner masses are m_1 and m_2, and their displacements are u_1 and u_2. The stiffness of the internal spring between m_1 and m_2 is k_2. The outer force acting on mass m_1 is F. To simplify the derivation of the governing equations of the RS, the mass of spring is ignored here. Then, Eq. (1) can be acquired based on the Newton's Second Law.

$$\begin{bmatrix} m_1 & 0 \\ 0 & m_2 \end{bmatrix} \begin{Bmatrix} \ddot{u}_1 \\ \ddot{u}_2 \end{Bmatrix} + \begin{bmatrix} k_2 & -k_2 \\ -k_2 & k_2 \end{bmatrix} \begin{Bmatrix} u_1 \\ u_2 \end{Bmatrix} = \begin{Bmatrix} F \\ 0 \end{Bmatrix} \tag{1}$$

Since the motion of effective mass m_{eff} of the microstructure is the same as the external mass m_1, the following Eq. (2) is always true.

$$m_{eff} = \frac{F}{\ddot{u}_1} \tag{2}$$

Assuming the outer force and mass motions are in a harmonic form, m_{eff} of the microstructure can be obtained as follows based on Eqs. (1) and (2).

$$m_{eff} = m_1 + \frac{\omega_2 m_2}{\omega_2^2 - \omega^2} \tag{3}$$

where $\omega_2 = \sqrt{k_2 / m_2}$ is resonant frequency of m_2. Then, the dimensionless effective mass m_{eff}/m_{st} of the microstructure can be obtained.

$$\frac{m_{eff}}{m_{st}} = 1 + \frac{\theta}{1+\theta}\left[\frac{(\omega/\omega_2)^2}{1-(\omega/\omega_2)^2}\right] \tag{4}$$

where m_{st} is the static mass of the microstructure and $\theta = m_2/m_1$ is the ratio of m_2 and m_1. Fig. 3 shows the plots of dimensionless effective mass m_{eff}/m_{st} and dimensionless frequency ω/ω_2 with different θ. Obviously, dimensionless effective mass m_{eff}/m_{st} is negative over a narrow frequency range, and this negative mass band gap can be applied to mitigate the waves [14, 15, 17]. Furthermore, the band gap becomes wider as θ increases. The increase of θ means the increase of m_1 or the decrease of m_2. Therefore, a heavy oscillator is beneficial to the attenuation effect of RSs.

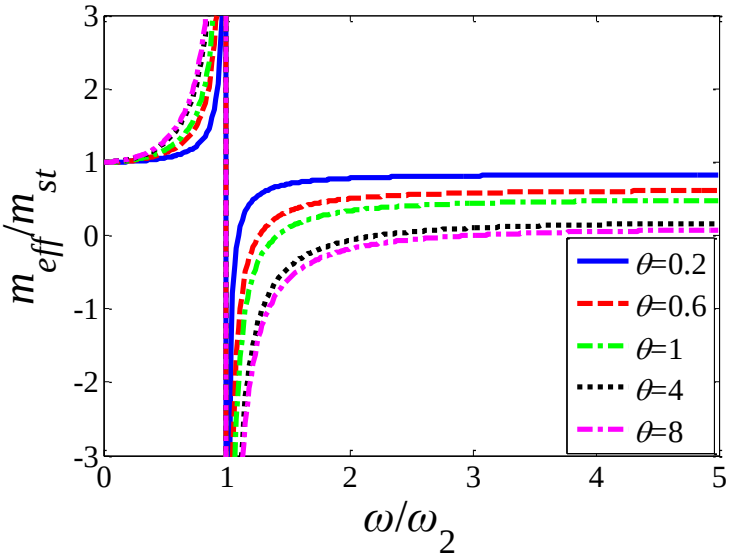

Fig. 3. Band gaps of m_{eff}/m_{st} and ω/ω_2 with different θ.

2.1.2 Study of attenuation effect of the composite material

Fig. 4 (a) shows the composite material under blast wave. From Fig. 4 (a), the blast wave is applied to the left side of the composite material. Periodic boundary condition is imposed on the four sides of the structure. The commercial software LSDYNA is applied to perform the impact analysis, and the analysis time is 3 μs.

Materials resin and steel are modeled by the piecewise linear plasticity material (No. 24) in the material library. In order to avoid stress wave reflection during the analysis, a 2mm PP resin material is added to the back end of the composite material. The entire model consists of 1983096 elements and 2040755 nodes. The pressures at sections 1 and 2 are selected as the output response. The resin material with the same geometry is applied to study the attenuation effect of the composite material. Fig. 4(b) shows the time-domain curve of the blast wave, and its overpressure is 5.3×10^{-3} GPa. Fig. 4(c) is the spectrum curve of the blast wave obtained by fast Fourier transform, and the frequency range is 0-2 MHz.

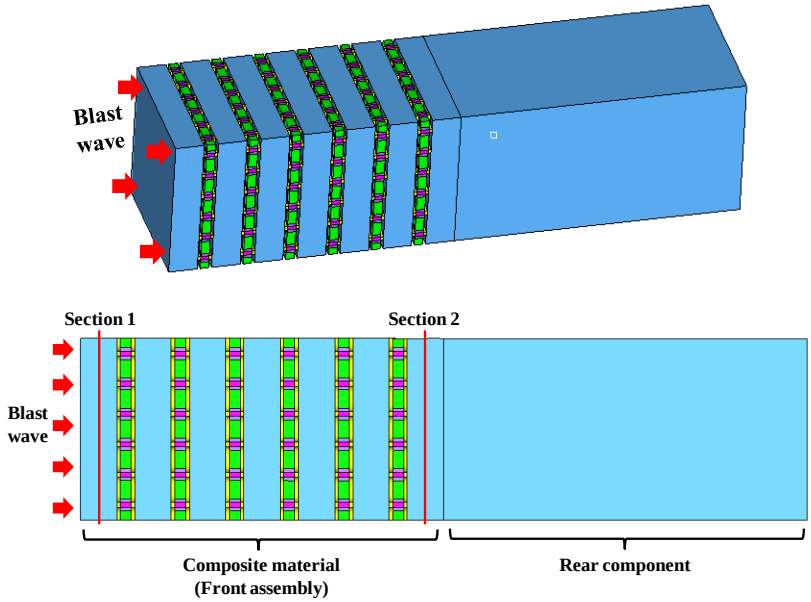

(a) The blast wave model

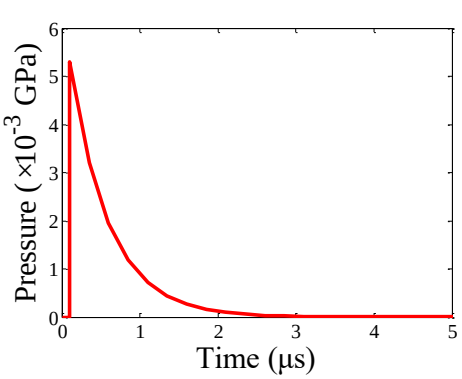

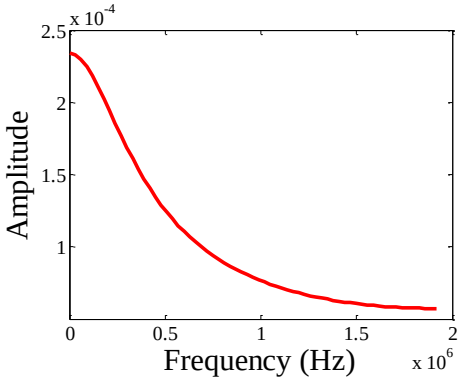

(b) Time-domain curve of blast wave (c) Spectrum curve of blast wave

Fig. 4. The composite material model with blast wave.

Fig. 5 illustrates the propagation of stress waves in the resin material and the composite material at different times (0.18μs, 0.29μs, 0.5μs, 0.99μs, 1.4μs, and 2.1μs).

In Fig. 5 (a), the stress waves are first generated in the impact region on the left side and then propagated in the resin material. The stress waves propagate to 0.2 mm at 0.18 μs and propagate to around 0.5 mm at 0.29 μs. In resin material, the propagation speed of stress waves is uniform, and the wave front is substantially in one plane. In addition, the stress amplitude in the propagation region is different. This indicates that there is periodic compression and stretching during the propagation of stress waves. When t = 0.99μs, the stress waves propagate through half of the whole structure. At this time, the stress in the material is mainly concentrated in the middle of the structure, and the propagation of stress waves begins to appear uneven. When t = 1.4μs, the wave front of stress waves reaches around 3 mm, and the stress waves in the material exhibit a significant wave behavior symmetrically along the X axis. There are two peak stresses at the left and right boundaries, and the wave front exhibits a slight convex shape. At t = 2.1μs, the wave front reaches the right border of the structure. Since the right boundary of the material is a free boundary, the stress is zero at the boundary. The stress waves exhibit a wavy behavior symmetrically along the X-axis, and there are three areas of stress concentration in the structure.

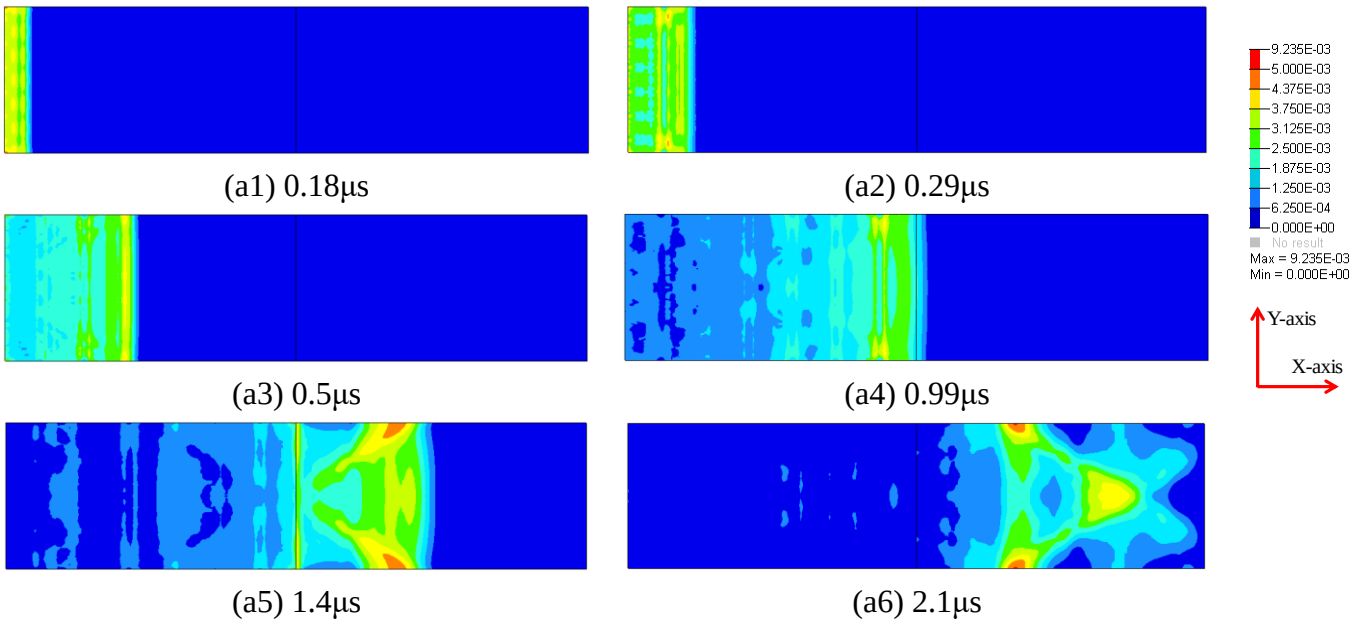

(a1) 0.18μs (a2) 0.29μs

(a3) 0.5μs (a4) 0.99μs

(a5) 1.4μs (a6) 2.1μs

(a) Pure resin model

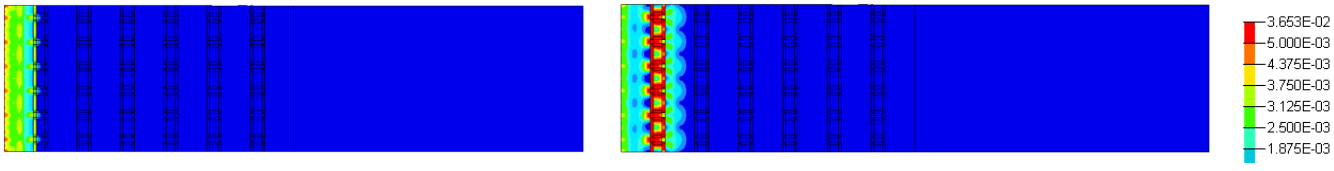

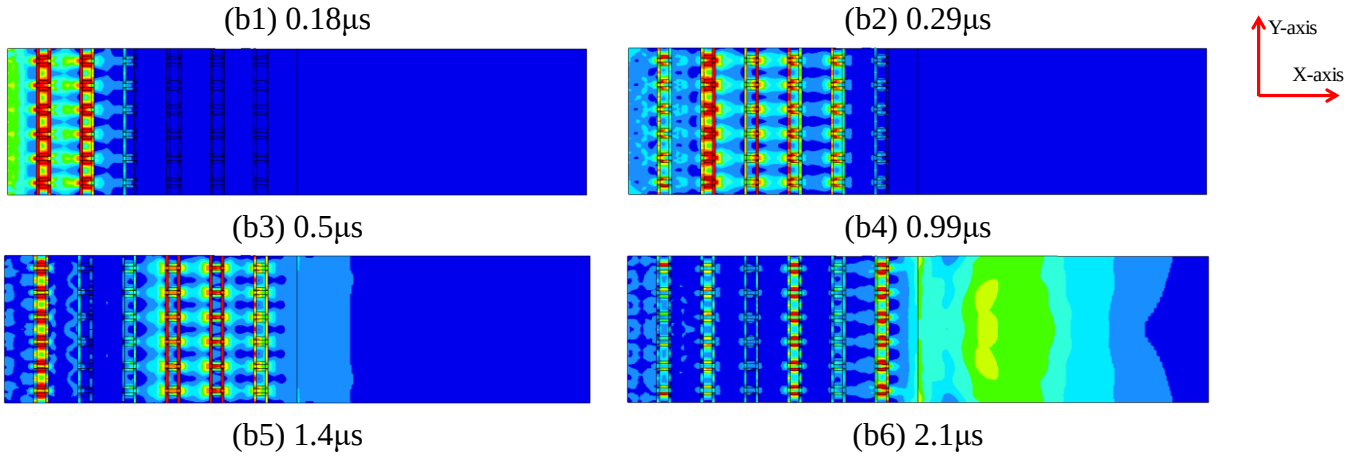

(b) Composite material model

Fig. 5. Stress nephograms of the pure resin and composite material models.

Fig. 6 (a) shows the internal energy and kinetic energy curves of the pure resin model. In Fig. 6 (a), both the internal energy and kinetic energy increase rapidly after the blast wave acts on the structure, and they have similar growth rates. At about 2.45μs, there is a sharp peak for the curve of kinetic energy and a marked valley for the curve of internal energy. This indicates that the stress waves have propagated to the end of the resin material, and these stress waves are reflecting. At this time, the internal energy of elasticity stored inside the material is converted into the kinetic energy. After 2.45 μs, the internal energy increases rapidly and the kinetic energy decreases quickly until they reach the inflection points. This means that the kinetic energy is further converted into the internal energy of elasticity of the material, after the reflection of the stress waves. Fig. 6 (b) illustrates the energy absorption of the front and rear components in the pure resin model, and the energy in this figure is a combination of internal energy and kinetic energy. From Fig. 6 (b), it can be seen that the energy stored in the front component increases rapidly first and then decreases quickly to a low level. The energy stored in the rear component begins to rise rapidly as the energy of the front component decreases, and it remains at a high level. This indicates that the stress waves propagate from front to back, and a high value of energy is generated in the front component. As the stress waves propagate to the rear component, the internal energy of elasticity and kinetic energy originally stored in the front component are released, and a large value of energy is generated in the rear component.

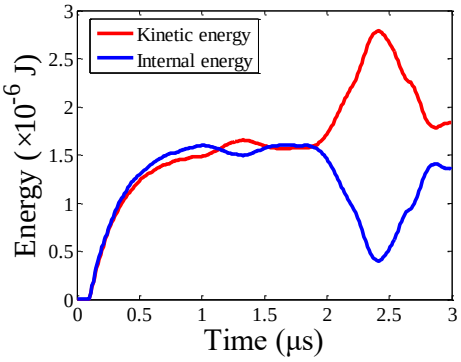

(a) Plots of internal energy and kinetic energy

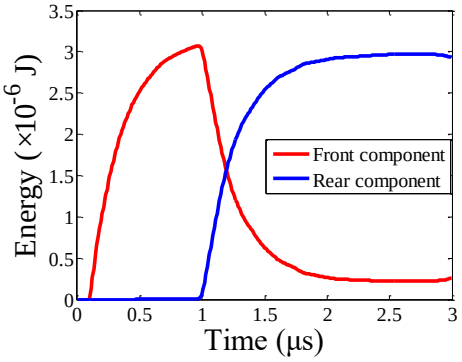

(b) Energy absorbed by the front and rear components

Fig. 6. Curves of energy absorbed by the pure resin model.

Unlike the propagation characteristics of stress waves in homogeneous resin material, the propagation of stress waves in composite material exhibits more complexity. As shown in Fig. 5 (b), the stress waves propagate to the first layer of RSs at 0.18 μs. At t = 0.29 μs, the stress concentration is obviously exhibited in the RSs and the connection area of the RSs and matrix structures, the peak stress of these regions is significantly greater than the matrix structure. In addition, the stress waves exhibit a periodic wave arc before and after the RSs. At t = 0.5 μs, the stress waves pass through the second layer of RSs, and its wave front reaches the third layer of RSs. The stress waves between the second and third layers of RSs exhibits a regular fan shape. When t = 0.99 μs, the stress waves just propagate to the last layer of RSs. At this point, the stress concentration is still mainly in the first five layer of RSs. Compared with the pure resin material, the obvious stress concentration phenomenon in composite material indicates that stress waves are constantly oscillated and reflected in the RSs, and the blast wave energy is significantly absorbed. When t = 1.4 μs, the stress waves pass through the middle region of the whole structure. At this time, the stress is mainly concentrated at the first, fourth, fifth and sixth layers of RSs, and the blast wave energy is still absorbed, stored and reflected by the sandwich structures. Finally, at t = 2.1 μs, the wave front approaches the right boundary of the structure, while the structural stress is still concentrated at the RSs.

Table 1 shows the numerical results of these two models. From Fig. 5 and Table 1, the peak stresses in the resin and composite material models are 9.24×10^{-3} GPa and

36.52×10^{-3} GPa. The structural stress is significantly concentrated in the interlayer regions of the RS, which indicates that the composite material can better absorb the blast wave energy compared with the pure resin material. In addition, it can be seen that the propagation velocity of stress waves in the pure resin material is greater than that of the composite material. The main reason is that the stress waves are continuously absorbed and reflected in these RSs.

Figs. 7 (a) and (b) show the curves of internal energy and kinetic energy of all parts in the composite material. In Fig. 7 (a), it is obvious that the internal energy of the parts is matrix, frame structure, coating and oscillator from large to small orderly. From Fig. 7 (b), the kinetic energy of the parts from large to small is oscillator, matrix, frame structure and coating orderly. Obviously, internal energy is mainly absorbed by matrix and frame structure, while kinetic energy is mainly stored in oscillator and matrix. The maximum kinetic energy of the oscillators (MEO) is 1.05×10^{-6} J. This means that a large part of the blast energy is converted into the kinetic energy of the oscillators. This indicates that the RSs can manipulate the impact energy through the resonant motions of the oscillators and alleviate the impact damage.

Figs. 7 (c) and (d) show the energy curves of the composite material model. From Fig. 7 (c), it can be seen that the curves of internal energy and kinetic energy always oscillate in a wave shape. This means that internal energy and kinetic energy are constantly transformed into each other. The main reason is that part of the energy carried by the stress waves is converted into the kinetic energy of the resonant motions of oscillators with the propagation of stress waves, and this part of kinetic energy are continuously released and absorbed, resulting in continuous conversion of internal energy and kinetic energy. In addition, the reflection time of the stress waves is about 2.8 μs, which is later than that of the pure resin model. This indicates that the propagation speed of stress waves in the composite material is slower than that of the resin. Fig. 7 (d) shows the energy absorbed by the composite material and the rear component. The energy absorbed by the composite material increases first and then decreases, and the energy absorbed by the rear component begins to increase as the energy of the composite material decreases. The phenomenon is caused by the reason

that is same as the pure resin material. The internal energy of elasticity and kinetic energy stored in the composite material are released as the stress waves propagate to the rear component, and the internal energy of plasticity is retained inside the composite material. From Figs. 6 (b), 7 (d) and Table 1, time of the intersection point of two energy curves of the front assembly and the rear component (TIE) in the composite material model is 1.87 μs, which is significantly larger than 1.19 μs of the pure resin model. This indicates that the storage time of the impact energy in the composite material is longer than that of the pure resin material, which is mainly because the energy absorption and conversion process caused by the resonant motions of oscillators reduces the propagation speed of the stress waves. The maximum energy absorbed by the front assembly (MEF) of the composite material and pure resin models are 3.68×10^{-6} J and 3.07×10^{-6} J, respectively. Their maximum energy absorbed by the rear component (MER) are 3.01×10^{-6} J and 2.98×10^{-6} J. The ratios of MER and MEF (RMM) of the composite material and pure resin models are 81.79 % and 97.07 %. A smaller value of RMM indicates a better energy absorption of the front assembly and a smaller proportion of the blast energy acting on the rear component. Obviously, the composite material model has a smaller value of RMM, which can absorb the impact energy better. In addition, from Figs. 6 (b), 7 (d) and Table 1, the internal energy of plasticity remaining in the front assembly (IPF) of the composite material and pure resin models are 0.67×10^{-6} J and 0.22×10^{-6} J. The ratios of IPF and MEF (RIM) of these two models are 81.79 % and 97.07 %, respectively. A larger RIM implies that the structure has a better energy absorption effect. Obviously, the value of RIM of the composite material is larger than that of the pure resin material, which also proves that the composite material can better absorb the impact energy, thereby protecting the rear structure. The energy absorption of the composite material also implies its attenuation effect of the pressure.

Figs. 7 (e) and (f) are the pressure curves at sections 1 and 2, and Table 1 shows the peak pressure of these two sections. From Figs. 7 (e), (f) and Table 1, the peak pressure at section 1 (PP1) of the resin and composite material models are 6.02×10^{-3} GPa, 6.78×10^{-3} GPa, and the peak pressure at section 2 (PP2) of these two models are

4.73×10^{-3} GPa and 3.69×10^{-3} GPa. It is obvious that the PP1 of the composite material model is larger than that of the resin model, while its PP2 is smaller. Furthermore, it can be seen from Fig. 7 that the pressure curve of the composite material at section 1 vibrates up and down along the pressure curve of the resin model, and the time of peak pressure of the composite material is significantly delayed compared with the resin model at section 2. The analysis results demonstrate that the RSs can effectively attenuate the BWR.

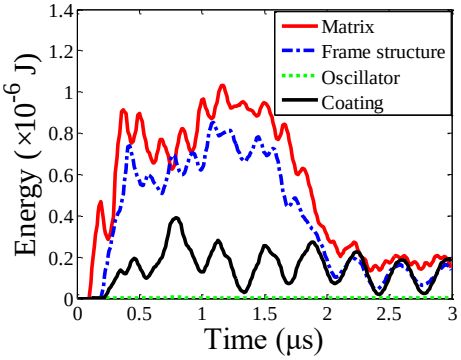

(a) Internal energy of each component in the composite material

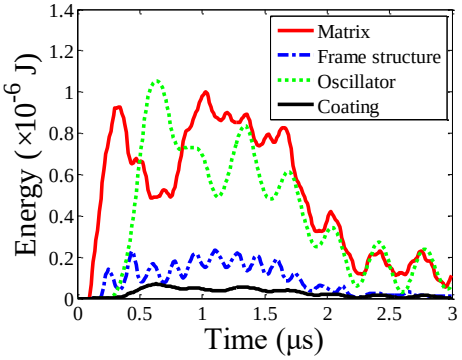

(b) Kinetic energy of each component in the composite material

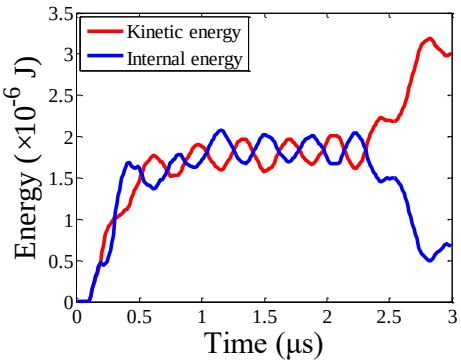

(c) Curves of internal energy and kinetic energy

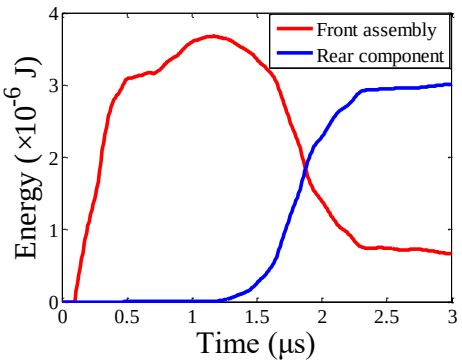

(d) Energy absorbed by the front assembly and the rear component

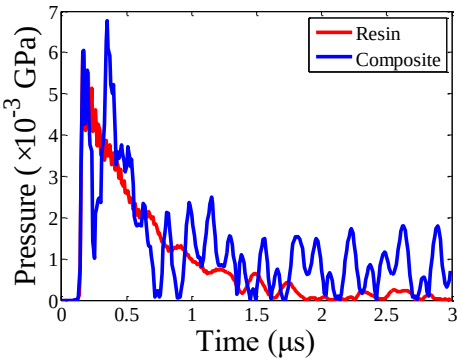

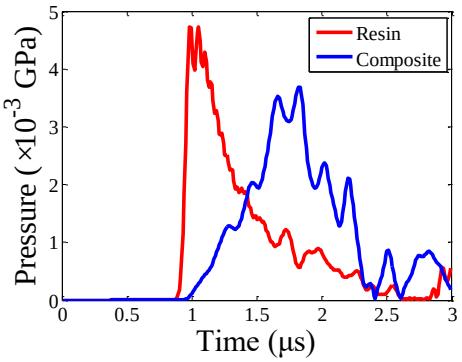

(e) Pressure at section 1 (f) Pressure at section 2

Fig. 7. Energy and pressure curves of the resin and composite material models.

Table 1. Dynamic responses of the resin and composite material models.

	PP1	PP2	Peak stress	MEF	MER	IPF	MEO	RMM	RIM	TIE
		($\times10^{-3}$ GPa)			($\times10^{-6}$ J)			(%)		(μs)
Resin	6.02	4.73	9.24	3.07	2.98	0.22	——	97.07	7.17	1.19
Composite material	6.78	3.69	36.53	3.68	3.01	0.67	1.05	81.79	18.21	1.87

Note: PP1 is the peak pressures at section 1, PP2 indicates the peak pressures at section 2, MEF stands for the maximum energy absorbed by the front assembly, MER denotes the maximum energy absorbed by the rear component, IPF represents the internal energy of plasticity remaining in the front assembly, MEO is the maximum kinetic energy of the oscillators, RMM is the ratio of MER and MEC, RIM denotes the ratio of IPF and MEF, and TIE means time of the intersection point of two energy curves of the front assembly and the rear component.

2.2 Analyses of materials of RSs on the performance of composite material

To better study the attenuation effect of RSs, the matching analyses of materials are conducted in this section. The combination of materials of RSs is shown in Table 2, and Table 3 is the parameters of each material.

2.2.1 Study of the coating materials

How the material of coating affects the attenuation effect of the composite material is studied first. As shown in Table 2, the coating materials of groups 1, 2 and 3 are resin, rubber and aluminum, and the materials of frame and oscillator structures in these groups are resin and steel. From Table 3, the modulus of the material is aluminum, resin and rubber from large to small orderly. We can study the effects of coating stiffness on the performance of the composite material, based on the analyses of these three groups. Ogden rubber model of material No. 77 in LSDYNA material library is applied to model the rubber material, and the parameters of the rubber material are shown in Table 4. The other materials in Table 3 are all modeled by the piecewise linear plasticity model of material No. 24 in the material library of LSDYNA.

Table 2. The combination of materials of the RSs.

	matrix	frame	coating	oscillator
group1	resin	resin	resin	steel
group2	resin	resin	rubber	steel
group3	resin	resin	aluminum	steel

group4	resin	resin	resin	resin
group5	resin	resin	resin	aluminum
group6	resin	resin	resin	copper
group7	resin	resin	resin	lead
group8	resin	resin	resin	gold

Table 3. Parameters of all materials.

material	E (Gpa)	ν	ρ (kg/m^3)
resin	1.2	0.33	1040
lead	16.0	0.42	11370
aluminum	70.0	0.33	2700
steel	207.0	0.30	7784
copper	110.0	0.33	8900
gold	85.0	0.42	19800

Table 4. Parameters of the ogden rubber model.

E ($\times 10^{-3}$ GPa)	ν	ρ (kg/m^3)	*N*	*NV*	*SGL*	*SW*	*ST*
0. 1175	0.496	1200	5	6	1	1	1

Fig. 8 and Table 5 show the computational results of the pressures, energy and structural stresses of the composite material models with coating materials of resin, rubber and aluminum, respectively. Figs. 8 (a1) and (b1) illustrate the kinetic energy curves of all components in the composite material of groups 2 and 3, respectively. For group 2, the kinetic energy of all components is matrix, frame structure, oscillator and coating in order from large to small. It is clear that the kinetic energy is mainly stored in the matrix. The kinetic energy of oscillators starts to increase at about 1.0 μs, and the rate of growth as well as the moment of onset are significantly slower than other three parts. The main reason is that the propagation speed of stress wave in rubber is significantly slower than other materials. Regarding group 3, the order of these components is matrix, oscillator, frame structure and coating. Obviously, the kinetic energy is mainly stored in the matrix and oscillator. A large amount of impact energy is converted into the kinetic energy of oscillators, which facilitates the absorption of impact energy and the attenuation of impact load. From Figs. 8 (a), (b) and Table 5, the values of MEO, RMM, RIM and TIE in group 2 are 0.34×10^{-6} J, 83.49 %, 17.69 % and 1.48 μs, and their values of group 3 are 0.75×10^{-6} J, 86.69 %, 14.16 % and 1.78 μs. Combining the results of group 1, it is clear that group 1 has the largest values of MEO, RIM and TIE, and the smallest value of RMM. Therefore, group 1 has the best manipulation effect of impact energy.

From Figs. 8 (c) and (d) as well as Table 5, the PP1 of groups 1, 2 and 3 are 6.78×10^{-3} GPa, 6.06×10^{-3} GPa and 7.48×10^{-3} GPa, respectively, and the PP2 are 3.67×10^{-3} GPa, 4.76×10^{-3} GPa and 3.78×10^{-3} GPa, respectively. The peak stress of structure is 36.53×10^{-3} GPa, 10.96×10^{-3} GPa and 50.44×10^{-3} GPa, respectively. It is obvious that the peak pressure and maximum structural stress of group 2 are comparable to those of the resin model. The peak pressures and the maximum structural stress of group 1 are all smaller than group 3. From Fig. 8 (a), the pressure curve of groups 1 - 3 at the section 1 vibrates up and down along the pressure curve of the resin model. The peak pressure of group 3 is the largest, the peak pressure of group 1 is slightly larger than that of the resin model, and the peak pressure of group 2 is comparable to the resin model. From Fig. 8 (b), the pressure curve of group 2 at section 2 is similar to the resin model. Their pressure amplitudes are close, while the time of peak pressure is relatively delayed. The main reason is that the structural stiffness of the rubber coating is weak, and the locally resonant frequency of the oscillator is low which cannot effectively attenuate the BWR. However, the low-frequency local resonance generated by the rubber coating can still reflect a small amount of stress waves, so the pressure curve at section 1 still fluctuates, and the PP2 is delayed slightly. Furthermore, the pressure curves of groups 1 and 3 at section 2 are close. Both of them lag behind the resin model significantly. The peak pressure of group 1 is slightly smaller than that of group 3. A smaller PP2 means a better attenuation effect. In addition, the resin coating is lighter than the aluminum coating. Therefore, the performance of group 1 is slightly better than that of group 3, and both groups 1 and 3 are significantly better than group 2. Based on the above analyses, reasonable coating stiffness has a positive effect on improving the performance of the composite materials.

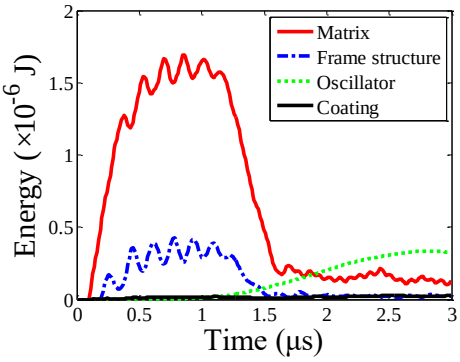

(a1) Kinetic energy of each component in the composite material

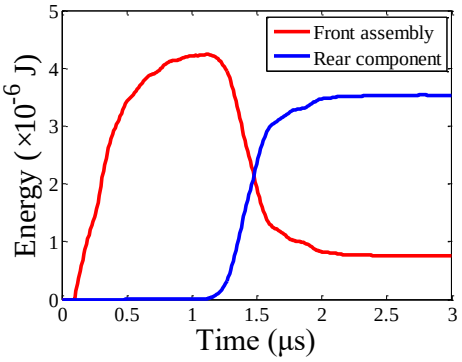

(a2) Energy absorbed by the front assembly and the rear component

(a) Rubber coating (group 2)

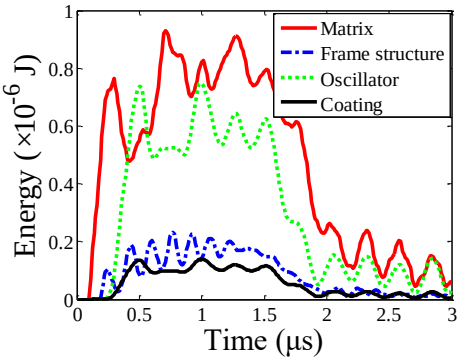

(b1) Kinetic energy of each component in the composite material

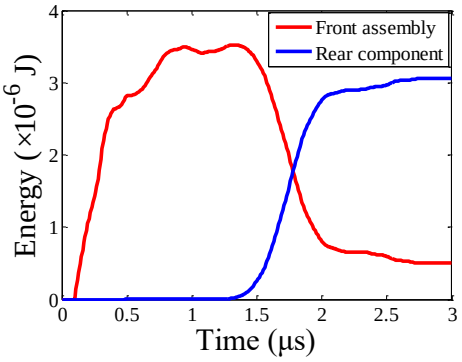

(b2) Energy absorbed by the front assembly and the rear component

(b) Aluminum coating (group 3)

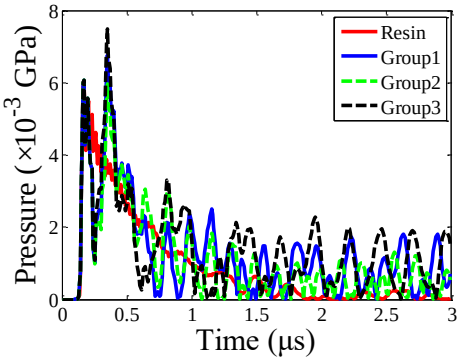

(c) Pressure at section 1

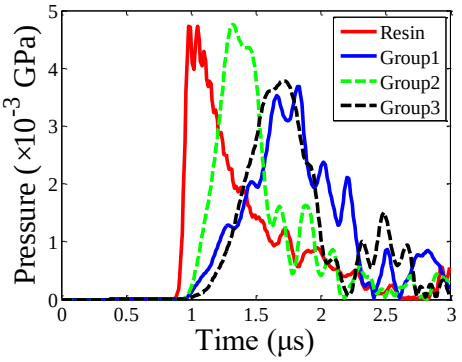

(d) Pressure at section 2

Fig. 8. Energy and pressure curves of the composite material models with different coating materials.

Fig. 9 (a) and (b) show the structural stress nephograms of the rubber and aluminum models at 0.29 μs, 0.99 μs, and 2.1 μs. In Fig.9 (a1), the stress waves propagate to the middle of the first interlayer and the second interlayer, causing stress concentration in the first interlayer region. In Fig.9 (a2), the stress waves propagate to

the sixth sandwich structure and the structural stress concentration is mainly concentrated at the fourth and fifth sandwich structures. From Fig.9 (a3), the stress wave front propagates to the rightmost region of the structure at 2.1μs. The stress wave propagation characteristic is symmetric along the X direction. At this time, there is no significant stress concentration in the sandwich structure. In Fig. 9 (b1), the stress waves pass through the first sandwich structure, and the stress concentration phenomenon in the first interlayer region is obvious. In Fig. 9 (b2), the stress waves propagate to the sixth sandwich structure, and the stress is mainly concentrated at the second, third and fourth layers. From Fig.9 (b3), the stress wave front propagates to the rightmost area of the structure at 2.1μs. At this time, a symmetrical wave phenomenon along the X direction appears in the resin material region, and the obvious stress concentration appears at the first, fourth and sixth layers. Compared with the structural stress nephograms of group 1, the stress concentration region of group 2 at the sandwich structure is smaller and the stress amplitude is lower. The stress concentration phenomenon of group 3 is similar to group 1. Considering the above results, the blast wave attenuation effect of group 2 is the worst.

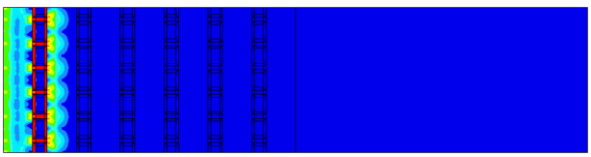

(a1) 0.29μs

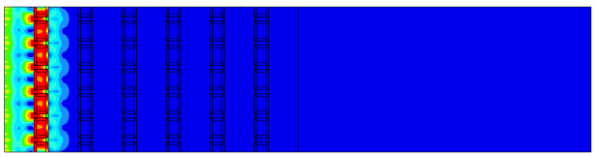

(b1) 0.29μs

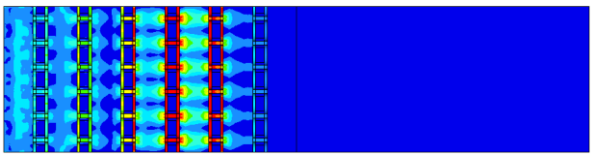

(a2) 0.99μs

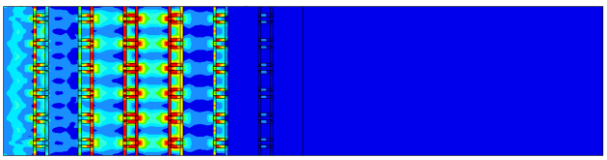

(b2) 0.99μs

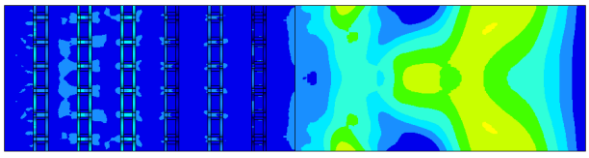

(a3) 2.1μs

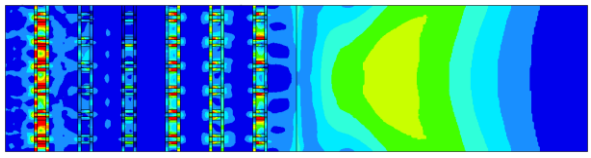

(b3) 2.1μs

(a) Rubber coating (group 2) (b) Aluminum coating (group 3)

Fig. 9. Stress nephograms of the composite material models with different coating materials.

Table 5. Responses of the composite material models of different groups.

	PP1	PP2	Peak stress	MEF	MER	IPF	MEO	RMM	RIM	TIE
			($\times 10^{-3}$ GPa)			($\times 10^{-6}$ J)			(%)	(μs)

Resin	6.02	4.73	9.24	3.07	2.98	0.22	——	97.07	7.17	1.19
Group 1	6.78	3.69	36.53	3.68	3.01	0.67	1.05	81.79	18.21	1.87
Group 2	6.06	4.76	10.96	4.24	3.54	0.75	0.34	83.49	17.69	1.48
Group 3	7.48	3.78	50.44	3.53	3.06	0.50	0.75	86.69	14.16	1.78
Group 4	6.18	5.03	13.45	4.12	3.94	0.28	0.16	95.63	6.80	1.50
Group 5	6.64	4.43	21.17	3.95	3.68	0.37	0.45	93.16	9.37	1.59
Group 6	6.75	3.63	36.53	3.63	2.89	0.73	1.16	79.61	20.11	1.92
Group 7	6.47	3.44	35.56	3.51	2.67	0.83	1.35	76.07	23.65	2.11
Group 8	6.68	2.81	36.69	3.20	2.11	1.08	1.55	65.94	33.75	2.45

Note: PP1 is the peak pressure at section 1, PP2 indicates the peak pressure at section 2, MEF stands for the maximum energy absorbed by the front assembly, MER denotes the maximum energy absorbed by the rear component, IPF represents the internal energy of plasticity remaining in the front assembly, MEO is the maximum kinetic energy of the oscillators, RMM is the ratio of MER and MEC, RIM denotes the ratio of IPF and MEF, and TIE means time of the intersection point of two energy curves of the front assembly and the rear component.

2.2.2 Study on the oscillator materials

Previous studies show that the attenuation of BWR requires a coating structure with reasonable stiffness. In this section, the effect of oscillator mass on the performance of the composite material is discussed. The materials of oscillator are selected as resin, aluminum, steel, copper, lead and gold, which correspond to groups 4, 5, 1, 6, 7 and 8 in Table 2, respectively. Obviously, the order of the density of these materials is resin < aluminum < steel < copper < lead < gold, which is the same as the order of the corresponding oscillator mass. The material parameters are shown in Table 3. In addition, the materials of matrix, frame and coating structures are all resin. Fig. 10 and Table 5 show the energy curves, pressure curves and numerical results of these groups. In Figs. 10 (a) - (e) and Table 5, the values of MEF, MER, IPF, MEO, RMM, RIM and TIE for group 4 are 4.12×10^{-6} J, 3.94×10^{-6} J, 0.28×10^{-6} J, 0.16×10^{-6} J, 95.63 %, 6.80 % and 1.50 μs. Regarding group 5, their values are 3.95×10^{-6} J, 3.68×10^{-6} J, 0.37×10^{-6} J, 0.45×10^{-6} J, 93.16 %, 9.37 % and 1.59 μs. Their values of group 6 are 3.63×10^{-6} J, 2.89×10^{-6} J, 0.73×10^{-6} J, 1.16×10^{-6} J, 79.61 %, 20.11 % and 1.92 μs, and their values of group 7 are 3.51×10^{-6} J, 2.67×10^{-6} J, 0.83×10^{-6} J, 1.35×10^{-6} J, 76.07 %, 23.65 % and 2.11 μs. For group 8, their values are 3.20×10^{-6} J, 2.11×10^{-6} J, 1.08×10^{-6} J, 1.55×10^{-6} J, 65.94 %, 33.75 % and 2.45 μs. Combining the results of group 1, it is obvious that with the increase of the mass of the oscillator, the

value of RMM decreases and the values of TIE, RIM and MEO increase. Therefore, the increase of mass of the oscillators is beneficial to the manipulation of impact energy by the composite material. From Figs. 10 (f), (g) and Table 5, it can be seen that the PP1 of groups 1, 4, 5, 6, 7 and 8 are 6.78×10^{-3} GPa, 6.18×10^{-3} GPa, 6.64×10^{-3} GPa, 6.75 ×10-3 GPa, 6.47 ×10-3 GPa and 6.68 ×10-3 GPa, respectively. Their PP2 are 3.69×10^{-3} GPa, 5.03×10^{-3} GPa, 4.43×10^{-3} GPa, 3.63×10^{-3} GPa, 3.44×10^{-3} GPa and 2.81×10^{-3} GPa. Their maximum structural stresses are 36.53×10^{-3} GPa, 13.45×10^{-3} GPa, 21.17×10^{-3} GPa, 36.53×10^{-3} GPa, 35.46×10^{-3} GPa and 36.69×10^{-3} GPa. Obviously, with the increase of oscillator density, the PP1 increases, the PP2 decreases, and the maximum structural stress increases. The results imply that the heavy oscillator is favorable for blast wave attenuation. In addition, from Fig. 10(b), the time of PP2 of these composite material models is delayed compared with the resin model. As the density of the oscillator increases, the delay is more pronounced. The above analysis results indicate that a better performance of the composite material requires a heavier oscillator, which is consistent with the conclusion of theoretical analysis in Section 2.1.1 where increasing θ can widen the band gap of the negative effective mass.

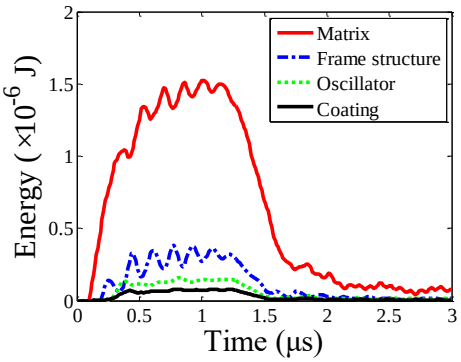

(a1) Kinetic energy of each component in the composite material

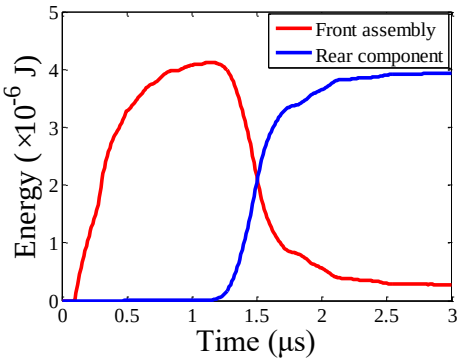

(a2) Energy absorbed by the front assembly and the rear component

(a) Resin oscillator (group 4)

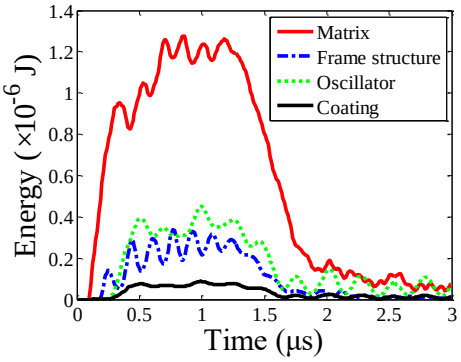

(b1) Kinetic energy of each component in the composite material

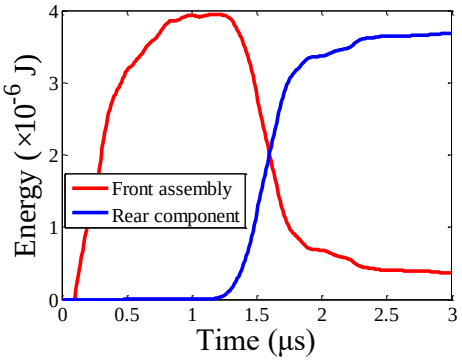

(b2) Energy absorbed by the front assembly and the rear component

(b) Aluminum oscillator (group 5)

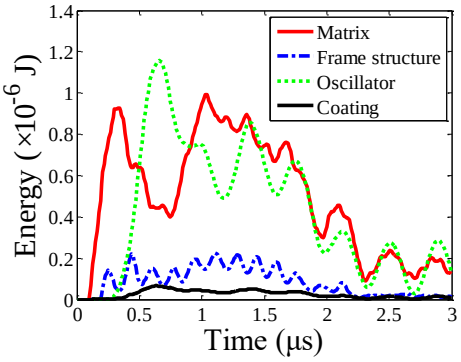

(c1) Kinetic energy of each component in the composite material

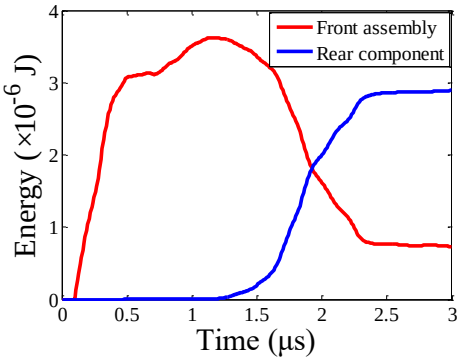

(c2) Energy absorbed by the front assembly and the rear component

(c) Copper oscillator (group 6)

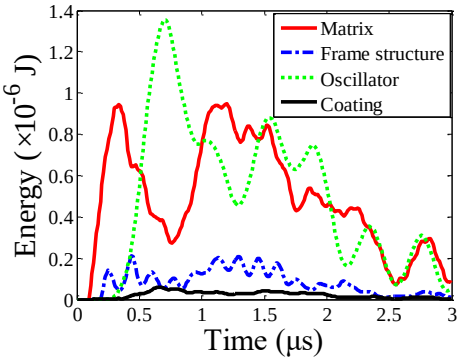

(d1) Kinetic energy of each component in the composite material

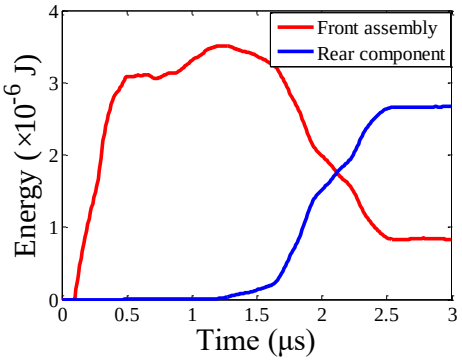

(d2) Energy absorbed by the front assembly and the rear component

(d) Lead oscillator (group 7)

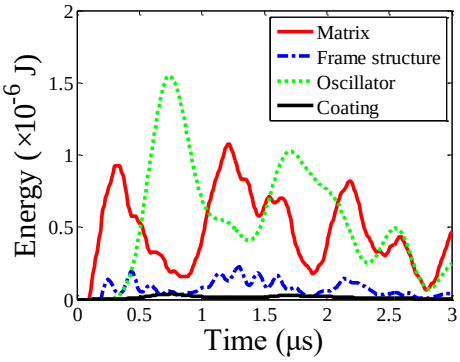

(e1) Kinetic energy of each component in the composite material

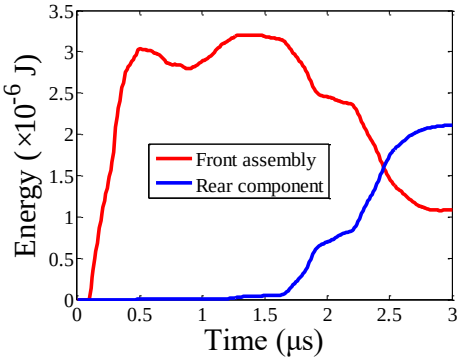

(e2) Energy absorbed by the front assembly and the rear component

(e) Gold oscillator (group 8)

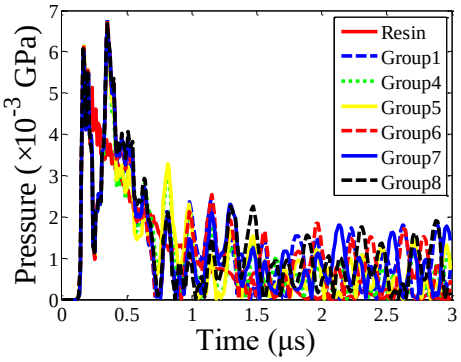

(f) Pressure at section 1

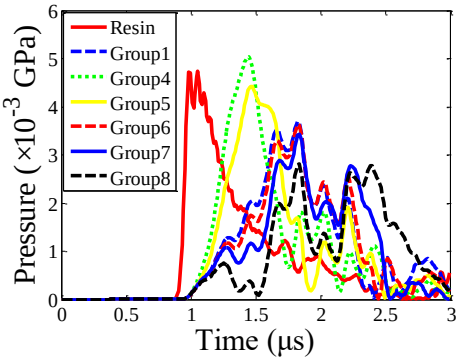

(g) Pressure at section 2

Fig. 10. Energy and pressure curves of the composite material models with different oscillator materials.

Figs. 11 (a), (b), (c), (d) and (e) are the stress nephograms of the composite material models with resin, aluminum, copper, lead, and gold oscillator, respectively. It is clear that as the density of the oscillator increases, the concentration of stress becomes more pronounced, while the propagation distance of the stress wave decreases. The results mean that the heavy oscillators can absorb and reflect the stress wave energy more effectively.

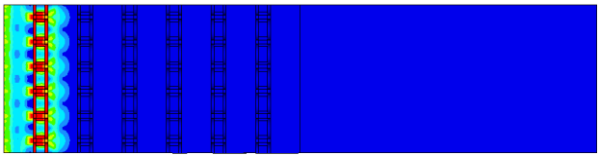

(a1) 0.29μs

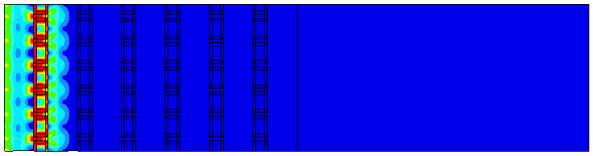

(b1) 0.29μs

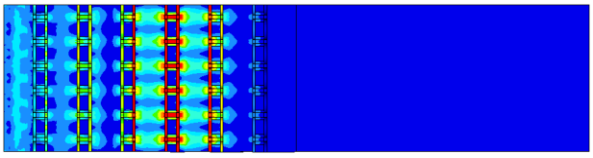

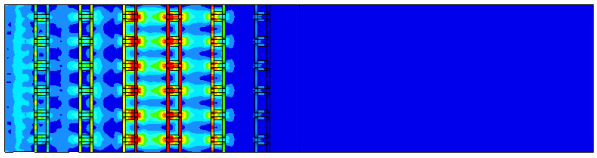

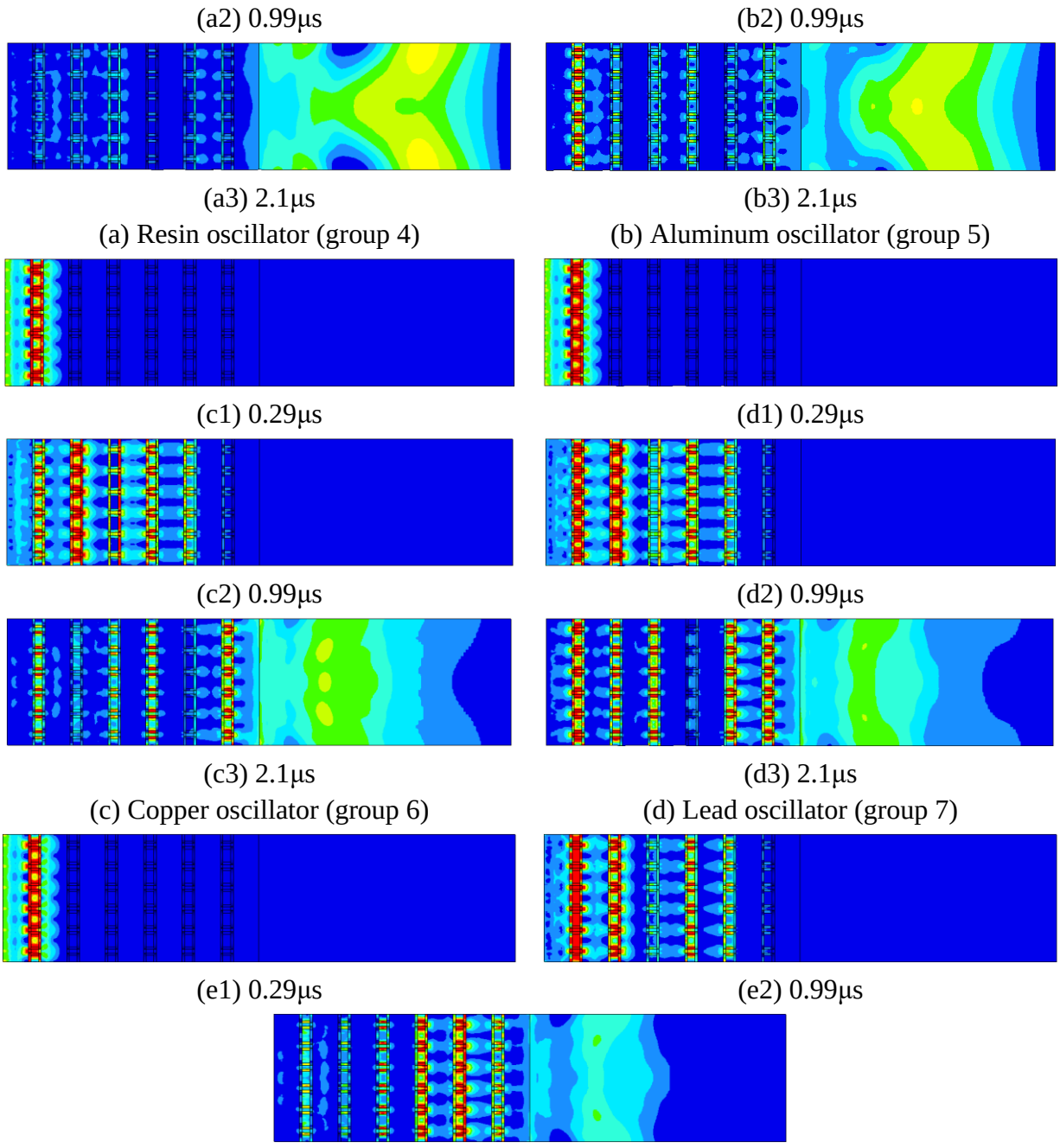

Fig. 11. Stress nephograms of the composite material models with different oscillator materials.

2.3 Attenuation effect of the composite material with improved RSs

In this section, redesign of the frame, oscillator and coating structures is applied to further enhance the attenuation effect of the RSs. Fig.12 shows the improved structure. Both sides of the structure are the resin matrix. The frame structure is in the middle of the matrix, and cylindrical holes are periodically arranged in the frame

structure. Six rows of oscillators and coatings are installed inside the cylindrical holes, and the pink area of the frame structure is the mounting region of the oscillator and coating. Compared with the original RSs, the changes of the improved RSs include: volume of the oscillator is increased, volume of the coating is reduced, layout of the coating is adjusted and five layers of matrix in the middle of the RSs is removed. These changes are beneficial to obtain a more reasonable coating stiffness and a heavier oscillator, which are conducive to improve the performance of the composite material. Meanwhile, deletion of excess matrix can make room for the RSs.

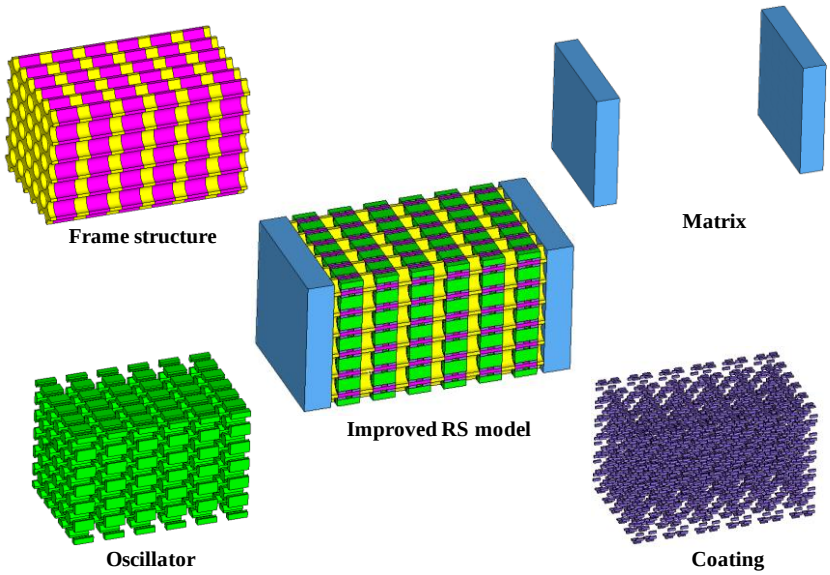

Fig. 12. The improved composite material model.

The detailed sizes of the improved oscillator and coating structures are shown in Fig. 13. From Fig. 13, the outer surface of the cylindrical oscillator is increased by four protruding structures to increase the structure mass. Diameter and length of the improved oscillator are 100 μm and 166.7 μm. The coating structure is changed to eight arcuate columnar structures which are arranged in the middle of the cylindrical convex structure. The length, width and height of one coating structure are 60 μm, 19.5 μm and 20 μm, respectively.

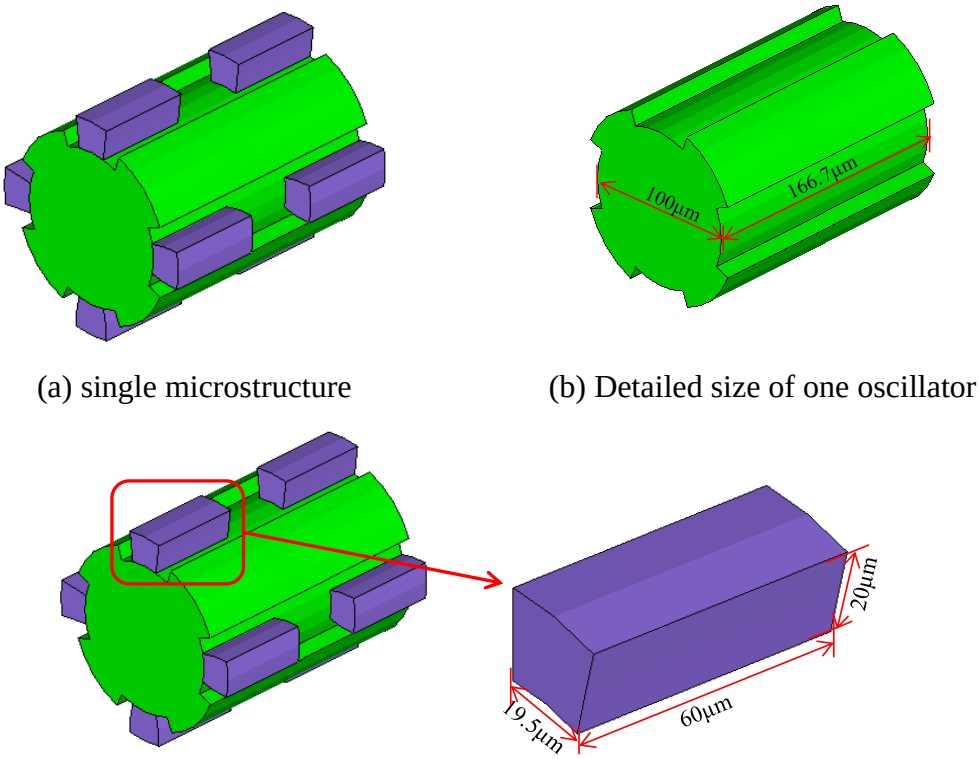

(a) single microstructure (b) Detailed size of one oscillator

(c) Detailed size of one coating

Fig. 13. Details of one improved RS.

Taking into account the performance of the RSs under different combination of material in the previous section as well as the weight of the structure, steel and resin are selected as the materials of oscillator and coating, respectively. The analysis time of this model is 3.5μs, and a 2mm resin material is also added to the back end of the RSs to avoid the reflection of stress wave. The entire model contains a total of 1775424 elements and 1864127 nodes.

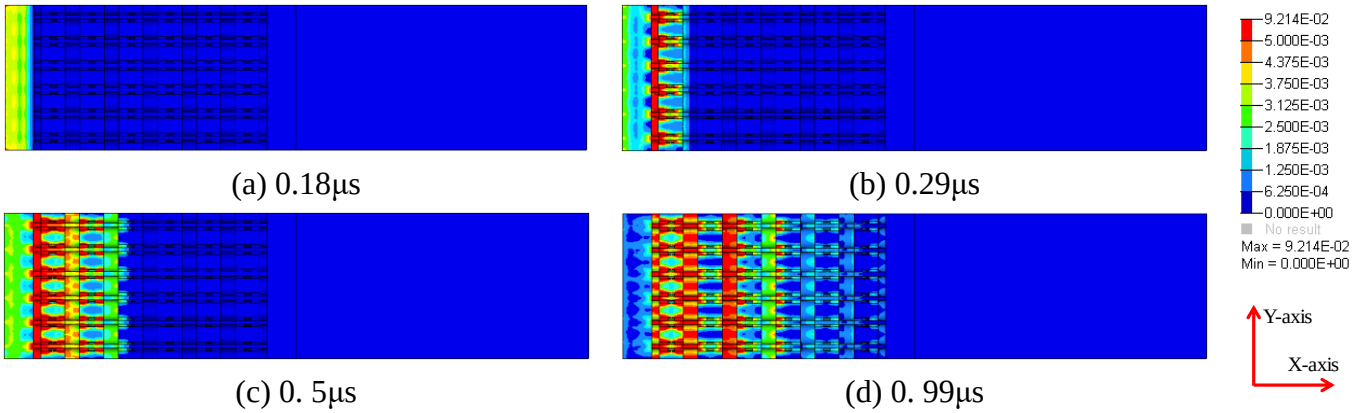

(a) 0.18μs (b) 0.29μs

(c) 0. 5μs (d) 0. 99μs

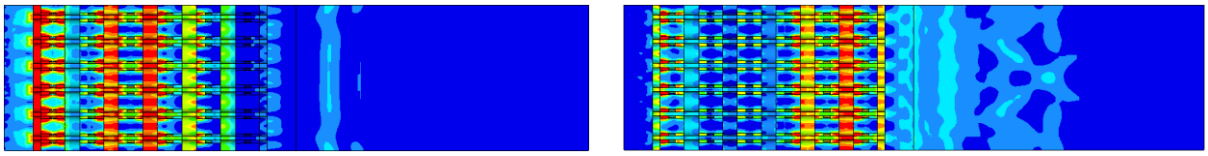

(e) 1.4μs (f) 2.1μs

Fig. 14. Stress nephograms of the improved RS model.

Fig. 14 shows the stress nephograms of the improved RS model at different times (0.18μs, 0.29μs, 0.5μs, 0.99μs, 1.4μs and 2.1μs). When t = 0.18 μs, the stress waves propagate to the sandwich structure. When t = 0.29 μs, the stress waves just pass through the first layer sandwich structure and produces a significant stress concentration phenomenon. When t = 0.5 μs, the stress waves propagate to the third layer, and the stress concentration region is significantly increased. When t = 0.99 μs, the stress wave front reaches the rightmost end of the frame structure and begins to propagate toward the resin matrix structure. The stress is mainly concentrated on the regions of the first, second, third and fourth layers of RSs. When t = 1.4 μs, the stress wave front reaches the structural region of about 2.5 mm, and stress fluctuation occurs in the resin structure. The stress concentration in the frame structure is still obvious. When t = 2.1 μs, the stress wave front reaches the position of about 3.2 mm, and the wave phenomenon which is symmetric along the X axis is generated in the resin structure. At this point, the stress amplitude of the resin structure is small, and the stress waves are still reflected back and forth within the frame structure. Throughout the analysis process, the maximum stress of the improved RS model is 92.14×10^{-3} GPa, which is significantly higher than that of the other composite material models in Section 2.2. This demonstrates that the blast wave attenuation effect of the improved RS model is enhanced.

Fig. 15 and Table 6 show the plots of energy and pressure as well as their numerical results of the improved RS model. From Fig. 15 (a), the internal energy is mainly absorbed by the frame structure and the coating, which is different from the composite material model in group 1. The main reason is the frame structure of the improved RS is different from the previous model. Fig. 15 (b) shows the kinetic energy of all components in the composite material. The value of MEO is 1.82×10^{-6} J,

which is significantly greater than that of the composite material in group 1. It is clear that the kinetic energy is mainly stored in the oscillators, which implies that the improved RS can efficiently manipulate the impact energy and alleviate the impact load. In Fig. 15 (c), the internal energy and kinetic energy curves continuously oscillate, and the amplitude of the oscillation is larger than that of group 1. At about 3.4 μs, there is a sharp peak in kinetic energy and a significant trough in internal energy. At this point, the stress waves have propagated to one end of the resin material, and these stress waves are reflecting. The reflection time of stress wave of the improved RS model is significantly later than the pure resin model and the group 1. This means that the stress wave energy is constantly converted inside the improved RS model, and the propagation speed of the stress waves is significantly reduced compared with the pure resin model and group 1. In Fig. 15 (d) and Table 6, the values of MEF, MER, IPF, RMM, RIM and TIE are 3.57×10^{-6} J, 2.34×10^{-6} J, 1.20×10^{-6} J, 65.54 %, 33.61 % and 2.67 μs. The value of RMM of the improved RS model is significantly smaller than the pure resin model and group 1, and its values of RIM and TIE are larger than those of group 1 and the pure resin model obviously. This means that the improved RS model absorbs a greater proportion of impact energy, which has a better protection for the rear component compared with group 1 and the pure resin. The large value of TIE of the improved RS model means the propagation speed of the stress waves is slow, and its ability to manipulate energy is stronger than that of group 1 and the pure resin model.

In Fig. 15 (e), (f), Tables 5 and 6, it can be seen that the PP1 of the improved RS model is 6.05×10^{-3} GPa, which is similar as the resin model. Its PP2 is 2.45×10^{-3} GPa, which is significantly less than the resin and other composite material models. In addition, the results in Fig. 15 (f) also show that the delay of the peak pressure moment of the improved RS model is more pronounced compared with the resin and other composite material models. This "delayed release" feature can be further used for other engineering problems. The overall analysis results demonstrate that the performance of the composite material is significantly improved with the redesign of the RS.

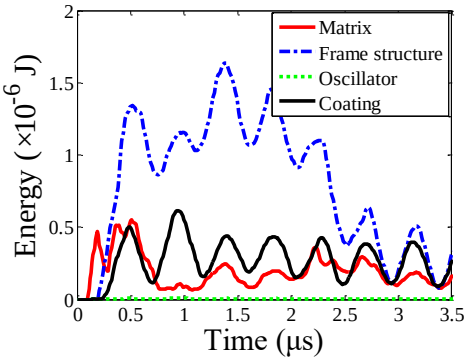

(a) Internal energy of each component in the composite material

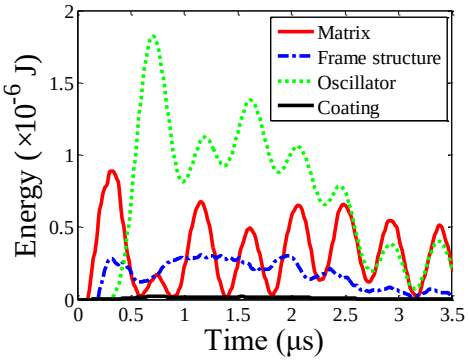

(b) Kinetic energy of each component in the composite material

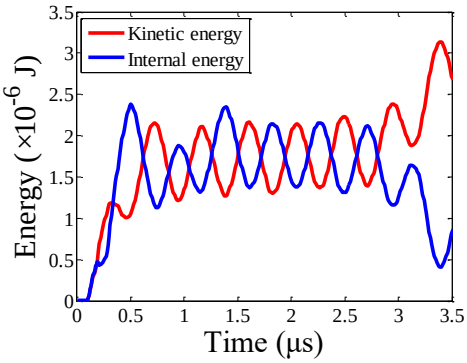

(c) Curves of internal energy and kinetic energy

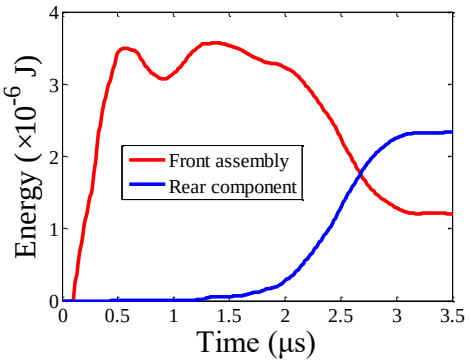

(d) Energy absorbed by the composite material and the rear component

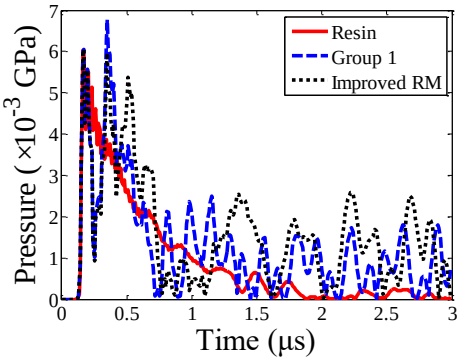

(e) Pressure at section 1

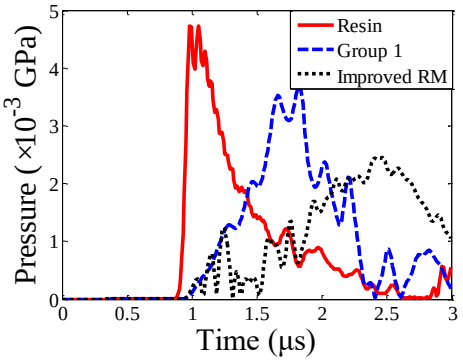

(f) Pressure at section 2

Fig. 15. Energy and pressure curves of the improved RS model.

Table 6. Dynamic responses of the improved RS model.

	PP1	PP2	Peak stress	MEF	MER	IPF	MEO	RMM	RIM	TIE
		($\times10^{-3}$ GPa)			($\times10^{-6}$ J)			(%)		(μs)
Resin	6.02	4.73	9.24	3.07	2.98	0.22	——	97.07	7.17	1.19
Group 1	6.78	3.69	36.53	3.68	3.01	0.67	1.05	81.79	18.21	1.87
Improved RS	6.05	2.45	92.14	3.57	2.34	1.2	1.82	65.54	33.61	2.67

Note: PP1 is the peak pressure at section 1, PP2 indicates the peak pressure at section 2, MEF stands for the maximum energy absorbed by the front assembly, MER denotes the maximum

energy absorbed by the rear component, IPF represents the internal energy of plasticity remaining in the front assembly, MEO is the maximum kinetic energy of the oscillators, RMM is the ratio of MER and MEC, RIM denotes the ratio of IPF and MEF, and TIE means time of the intersection point of two energy curves of the front assembly and the rear component.

3 Parameter reverse of the WNLS

The improved RS model in Section 2.3 is selected as the original model to study the attenuation effect of blast wave at the macro-scale. Since this composite material contain too much element and node, it is very difficult to construct the macro-scale model by directly combining its micro-scale information. It is necessary to simplify the three-dimensional composite material model. Scholars had studied the linear and nonlinear one-dimensional lattice systems [31-34] which has the advantages of simple principle, less parameters and high computational efficiency. Since the analysis model is a nonlinear impact model, a one-dimensional WNLS is applied to approximate the attenuation effect of the composite material to reduce the computational cost.

3.1 The mathematical model of the WNLS

As shown in Fig. 16, an equivalent model of the improved RS model is built based on the WNLS. In Fig. 16, the light blue parts on both sides are the matrix, and the middle part is the WNLS. There are six single-resonator microstructures in this WNLS. Each microstructure is linked by two external nonlinear springs which stiffness is controlled by two parameters, and the nonlinearity of spring is described by a polynomial. For this weak nonlinearity model, a small parameter ε is introduced to simulate the restoring force of the outer spring. The spring stiffness k_1 and restoring force F_1 can be written as Eqs. (5) and (6).

$$k_1 = b_1 + \varepsilon b_2 x^2 \tag{5}$$

$$F_1 = b_1 x + \varepsilon b_2 x^3 \tag{6}$$

where x is the deformation of the outer spring, b_1 and b_2 are the linear and nonlinear stiffness parameters. The governing equations of the lattice system can be written as follows.

$$m_1\ddot{u}_1^{(j)} = b_1(u_1^{(j-1)} + u_1^{(j+1)} - 2u_1^{(j)}) + \varepsilon b_2[(u_1^{(j-1)} - u_1^{(j)})^3 + (u_1^{(j+1)} - u_1^{(j)})^3] + k_2(u_2^{(j)} - u_1^{(j)}) \tag{7}$$

$$m_2\ddot{u}_2^{(j)} = k_2(u_1^{(j)} - u_2^{(j)}) \tag{8}$$

where $u_2^{(j)}$ and $u_1^{(j)}$ are the displacements of the inner and outer masses of *j*-th cell. Then, Eqs. (7) and (8) can be updated as follows.

$$\frac{\theta_2}{\delta_2\omega_2^2}\ddot{u}_1^{(j)} = (u_1^{(j-1)} + u_1^{(j+1)} - 2u_1^{(j)}) + \varepsilon\delta_1[(u_1^{(j-1)} - u_1^{(j)})^3 + (u_1^{(j+1)} - u_1^{(j)})^3] + \delta_2(u_2^{(j)} - u_1^{(j)}) \tag{9}$$

$$\frac{\ddot{u}_2^{(j)}}{\omega_2^2} = (u_1^{(j)} - u_2^{(j)}) \tag{10}$$

where $\delta_2 = k_2/b_1$ and $\delta_1 = b_2/b_1$ is the ratio of stiffness parameters. Next, Eqs. (9) and (10) can be rewritten as Eqs. (11) and (12) through the defining of dimensionless time $\tau = \omega t$ and dimensionless frequency $\Omega = \sqrt{\omega^2/\omega_2^2}$.

$$\frac{\delta_2\Omega^2}{\theta_2}\frac{\partial^2 u_1^{(j)}}{\partial\tau^2} = (u_1^{(j-1)} + u_1^{(j+1)} - 2u_1^{(j)}) + \varepsilon\delta_1[(u_1^{(j-1)} - u_1^{(j)})^3 + (u_1^{(j+1)} - u_1^{(j)})^3] + \delta_2(u_2^{(j)} - u_1^{(j)}) \tag{11}$$

$$\Omega^2\frac{\partial^2 u_2^{(j)}}{\partial\tau^2} = (u_1^{(j)} - u_2^{(j)}) \tag{12}$$

The perturbation approach [33, 35] is applied to acquire the dispersion equation of the WNLS. As shown in Eq. (13), the disturbances of $u_1^{(j)}$, $u_2^{(j)}$ and Ω expand to the first order.

$$u_1^{(j)} = u_{1(0)}^{(j)} + \varepsilon u_{1(1)}^{(j)} \quad u_2^{(j)} = u_{2(0)}^{(j)} + \varepsilon u_{2(1)}^{(j)} \quad \Omega = \Omega_0 + \varepsilon\Omega_1 \tag{13}$$

Eq. (13) is substituted into Eqs. (11) and (12), and the coefficients of ε^0 and ε^1 are extracted separately. Then, the governing equations Eqs. (11) and (12) can be rewritten as follows.

$$\frac{\delta_2\Omega_0^2}{\theta_2}\frac{d^2 u_{1(\alpha)}^{(j)}}{d\tau^2} - (u_{1(\alpha)}^{(j-1)} + u_{1(\alpha)}^{(j+1)} - 2u_{1(\alpha)}^{(j)}) - \delta_2(u_{2(\alpha)}^{(j)} - u_{1(\alpha)}^{(j)}) = O_\alpha \tag{14}$$

$$\Omega_0^2\frac{d^2 u_{2(\alpha)}^{(j)}}{d\tau^2} - (u_{1(\alpha)}^{(j)} - u_{2(\alpha)}^{(j)}) = P_\alpha \tag{15}$$

where subscript $\alpha = 0, 1$ corresponds to ε^0 and ε^1 respectively. O_α and P_α are written as follows.

$$O_0 = 0 \quad P_0 = 0 \tag{16}$$

$$O_1 = -2\frac{\delta_2}{\theta_2}\Omega_0\Omega_1\frac{d^2u_{1(0)}^{(j)}}{d\tau^2} + \delta_1[(u_{1(0)}^{(j-1)} - u_{1(0)}^{(j)})^3 + (u_{1(0)}^{(j+1)} - u_{1(0)}^{(j)})^3] \tag{17}$$

$$P_1 = -2\Omega_0\Omega_1\frac{d^2u_{2(0)}^{(j)}}{d\tau^2} \tag{18}$$

The governing equation of the linear lattice system is recovered by the lowest order. With nonlinear terms serving as the forcing function, the higher order expansion is a heterogeneous form of the linear system. Through the requirement of non-long-term solutions, the correction of frequency for each order nonlinearity is acquired. Assume that the solutions of the linear lattice system are as follows.

$$u_{1(0)}^{(j)} = \frac{H_1}{2}e^{inqa}e^{i\tau} + c \tag{19}$$

$$u_{2(0)}^{(j)} = \frac{H_2}{2}e^{inqa}e^{i\tau} + c \tag{20}$$

where a and q is the lattice constant and wavenumber, c represents the complex conjugate. H_1 and H_2 denote the amplitudes of the external and internal masses, respectively. The following equations can be obtained by substituting Eqs. (19) and (20) into Eqs. (14) and (15).

$$\{(1-\Omega_0^2)[-\delta_2\Omega_0^2 + 2\theta_2(1-\cos(qa))] - \delta_2\theta_2\Omega_0^2\}H_1 = 0 \tag{21}$$

$$H_2 = \frac{H_1}{1-\Omega_0^2} \tag{22}$$

Then, the dispersion function of the linear lattice system can be obtained as follows.

$$\{(1-\Omega_0^2)[-\delta_2\Omega_0^2 + 2\theta_2(1-\cos(qa))] - \delta_2\theta_2\Omega_0^2\} = 0 \tag{23}$$

From Eq. (23), two positive real roots can be obtained as follows.

$$\Omega_{0ac} = \sqrt{\frac{K - \sqrt{K^2 - 8\delta_2\theta_2(1-\cos(qa))}}{2\delta_2}} \tag{24}$$

$$\Omega_{0om} = \sqrt{\frac{K + \sqrt{K^2 - 8\delta_2\theta_2(1-\cos(qa))}}{2\delta_2}} \tag{25}$$

where $K = \delta_2 + \delta_2\theta_2 + 2\theta_2(1-\cos(qa))$, Ω_{0am} is the smaller root which corresponds to the acoustic mode, and Ω_{0om} is the larger root that corresponds to the optical mode [33]. For α = 1, the governing equations of the WNLS can be updated as follows.

$$\begin{aligned}&(\Omega_0^2\frac{d^2}{d\tau^2}+1)[\frac{\delta_2}{\theta_2}\Omega_0^2\frac{d^2u_{1(1)}^j}{d\tau^2}+(2u_{1(1)}^j-u_{1(1)}^{j-1}-u_{1(1)}^{j+1})]+\delta_2\Omega_0^2\frac{d^2u_{1(1)}^j}{d\tau^2}\\&=c_1e^{inqa}e^{i\tau}+c_2e^{3inqa}e^{3i\tau}+c\end{aligned} \tag{26}$$

$$(\Omega_0^2\frac{d^2}{d\tau^2}+1)u_{2(1)}^j=\Omega_0\Omega_1\frac{H_1}{1-\Omega_0^2}e^{inqa}e^{i\tau}+u_{1(1)}^j \tag{27}$$

where

$$c_1=(1-\Omega_0^2)[\frac{\delta_2}{\theta_2}\Omega_0\Omega_1H_1-1.5\delta_1(1-\cos(qa))^2H_1^2H_1^*]+\delta_2\Omega_0\Omega_1\frac{H_1}{1-\Omega_0^2}$$

$$c_2=0.5\delta_1(\delta_2-9\frac{\delta_2}{\theta_2}\Omega_0^2)(2\cos^3(qa)+3\cos^2(qa)-1)H_1^3$$

In the equation of c_1, the asterisk indicates the complex conjugate. The forced term e^{inqa} on the right side the equal sign of Eq. (26) is long-term and must be removed. Then, the following equation can be obtained by setting $c_1 = 0$.

$$\Omega_1=\frac{3\delta_1(1-\cos(qa))^2|H_1|^2}{2\Omega_0(\delta_2+\theta_2\delta_2/(1-\Omega_0^2)^2)} \tag{28}$$

Finally, the dispersion relation of this WNLS is reconstituted as follows.

$$\Omega_{am}=\Omega_{0ac}+\varepsilon\frac{3\delta_1(1-\cos(qa))^2|H_1|^2}{2\Omega_{0ac}(\delta_2+\theta_2\delta_2/(1-\Omega_{0ac}^2)^2)} \tag{29}$$

$$\Omega_{om}=\Omega_{0om}+\varepsilon\frac{3\delta_1(1-\cos(qa))^2|H_1|^2}{2\Omega_{0om}(\delta_2+\theta_2\delta_2/(1-\Omega_{0om}^2)^2)} \tag{30}$$

The dispersion curves of WNLS and linear lattice system obtained by the perturbation approach [33, 35] are shown in Fig. 17. The dimensionless parameters are set as θ_2 = 1 and δ_2 = 1. The nonlinear parameters are selected as $\varepsilon\delta_1|H_1|^2$ = 0.02, $\varepsilon\delta_1|H_1|^2$ = 0.1, $\varepsilon\delta_1|H_1|^2$ = 0.2 and $\varepsilon\delta_1|H_1|^2$ = 0, respectively, to describe the WNLS and the linear lattice system. From Fig. 17, it is seen that both the WNLS and the linear lattice

system have a band gap. The shaded area in Fig. 17 is the band gap of $\varepsilon\delta_1|H_1|^2 = 0.02$. The band gap of the linear lattice system is slightly different from the WNLS, and these band gaps can be applied to manipulate the propagation of waves. As the nonlinear parameter $\varepsilon\delta_1|H_1|^2$ increases, the band gap width of the WNLS decreases. In this work, we design the spring stiffness parameters of the WNLS to adjust its band gap and its attenuation effect, so that the performance of the WNLS can approximates the improved RS model well.

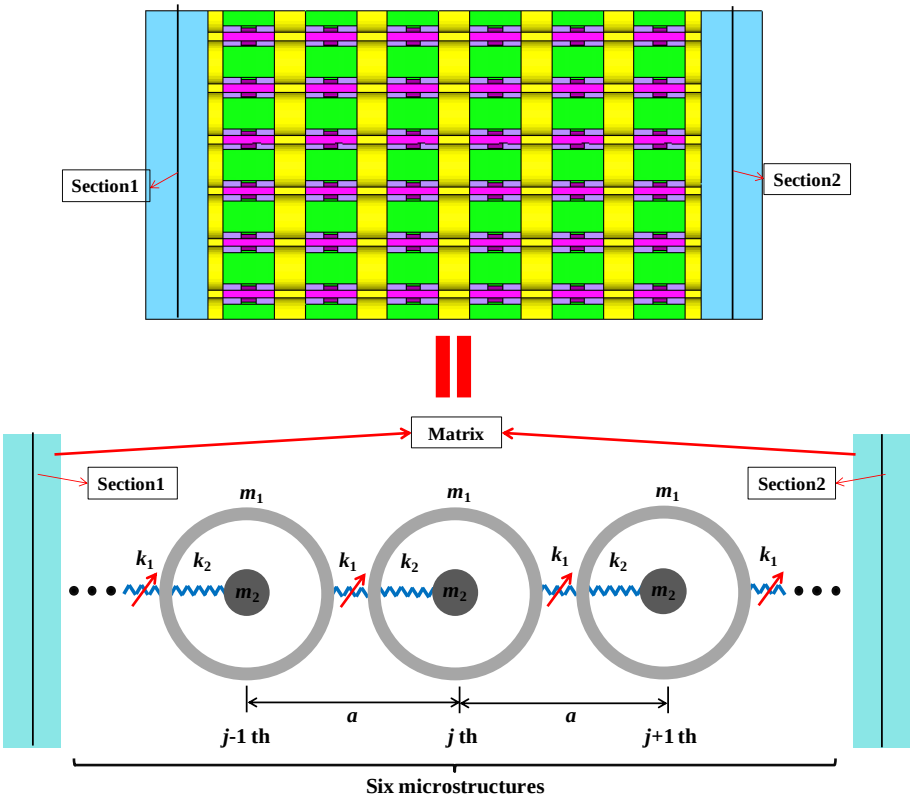

Fig. 16. The equivalent model of the composite material with improved RSs.

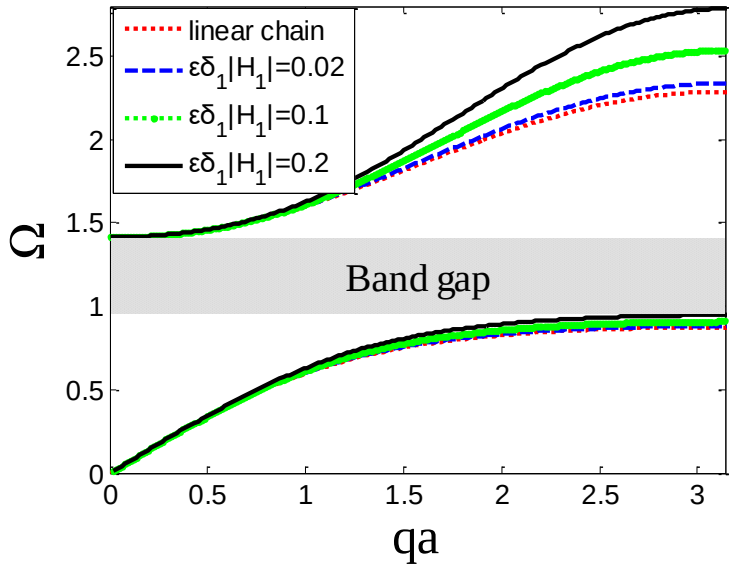

Fig. 17. Dispersion curves of the WNLS and the linear lattice system.

3.2 Parameters reverse of the WNLS based on AT algorithm

In Fig. 16, total mass of this equivalent model is 3.92×10^{-6} kg which is equal to the improved RS model. The masses of the matrix and the WNLS are 0.416×10^{-6} kg and 3.51×10^{-6} kg, respectively. The outer and internal masses of one microstructure are $m_1 = m_2 = 0.2925\times10^{-6}$ kg. The pressures of the equivalent and improved RS models at sections 1 and 2 are the output responses. The fit of the response curves between these two models is defined as the target. The IGD metric [36] is applied to evaluate the fit. A small IGD value means a better fit. The design variables of the equivalent model are the inner and outer spring stiffness parameters b_1, b_2 and k_2. Table 7 shows the design space of these parameters. Since the calculation results are the pressure curves at sections 1 and 2, there are two IGD values (IGD_1 and IGD_2) that corresponding to the responses at sections 1 and 2. Based on AT algorithm [37, 38], the inverse of the spring stiffness parameters is carried out with the goal of minimizing the $IGD = IGD_1 + IGD_2$.

AT is an efficient heuristic algorithm that was proposed by Li et al. in 2017. Fig. 18 shows the optimization flow of AT. In AT, the positions of the branches represent the design variables, and the branches themselves are the solutions of the optimization problem. A thicker branch means a better solution. Two evolutionary operators of

branches are applied to update the solutions which are the crossover and self-evolution operators. Through the execution of all operations in the algorithm, AT can efficiently solve a variety of optimization problems.

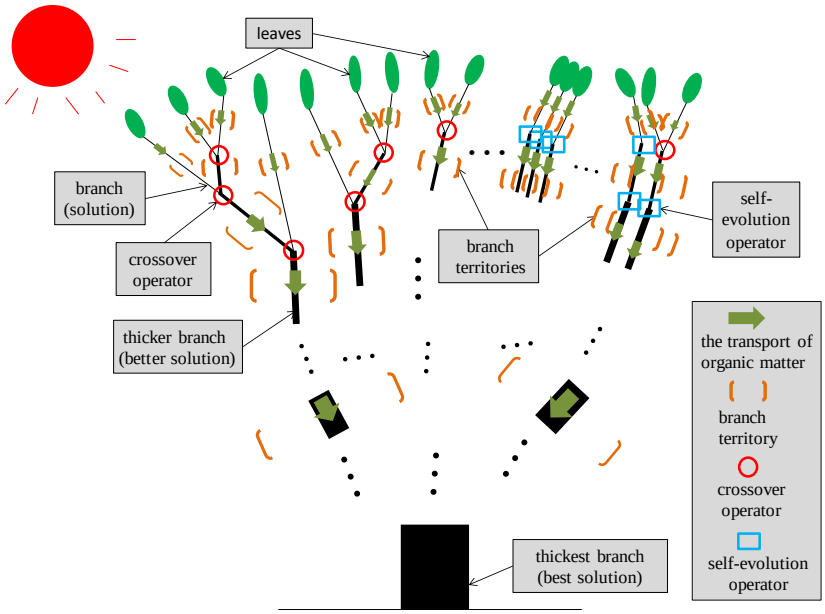

Fig. 18. The bio-inspired model of AT.

Fig. 19 illustrates the pressure curves of the improved RS and equivalent models. In Fig. 19 (a), at section 1, the peak pressure, peak pressure moment and curve form of the equivalent model are consistent with the improved RS model before 1μs. From Fig. 19 (b), at section 2, the rise and fall speed as well as the amplitude and amplitude moment of the pressure curves between these two models are very consistent. Table 8 shows the optimized spring stiffness parameters and the IGD values. The values of IGD_1 and IGD_2 are reduced from 0.25 and 0.34 to 0.105 and 0.0029. Therefore, the equivalent model can approximate the response of the improved RS model very well, which can replace the real model to construct the macro-scale composite material model.

Table 7. Design space of the spring stiffness parameters.

	b_1	b_2	k_2
Initial value	1	1	1
Lower limit	1	1	1
Upper limit	100	100	100

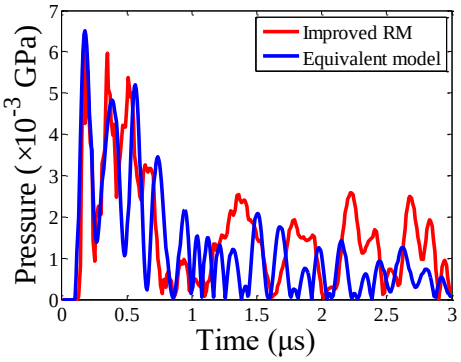

(a) Pressure at section 1

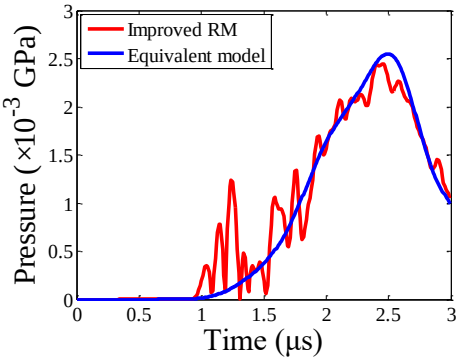

(b) Pressure at section 2

Fig. 19. Pressure curves of the improved RS and equivalent models.

Table 8. The spring stiffness parameters of the equivalent model.

	b_1	b_2	k_2	IGD_1	IGD_2
Initial value	1	1	1	0.25	0.34
Designed value	7.989	7.005	10.763	0.105	0.0029

4 Attenuation effect of the macro-scale composite material plate structure

The macro-scale composite material plate structure is established based on the equivalent model. Fig. 20 shows the geometry of the macro-scale composite material model. This model is a square plate structure with a side length of 192 mm, a plate thickness of 2 mm, and a structural mass of 0.145 kg. The model contains 847,892 elements and 960,794 nodes. Dynamic response of a three-dimensional block rubber material under the blast wave is studied to test the attenuation effect of the composite material. Fig. 21 (a) shows the block rubber material which has a rectangular structure with length, width and height of 190 mm, 190 mm and 100 mm, respectively. In addition, traditional materials of resin, aluminum alloy and steel are also applied to evaluate the performance of the macro-scale composite material plate. Structures of the traditional materials are also the square plate with a side length of 192 mm. Three cases are applied. The first case is to directly apply the blast wave to the rubber material. The second one is that the blast wave is applied to the traditional material plate structure while placing the rubber material behind the traditional material. The third case is to apply the blast wave to the composite material plate structure while placing the rubber material behind the composite material. Two contrasting methods are applied. The first is to set the same mass for traditional material and composite

material models. The second one is that plate thicknesses of traditional material and composite material models are the same. The thicknesses of traditional material models can be acquired based on the above two contrasting. Figs. 21 (b) and (c) show the rubber material with traditional material and composite material plate structures, respectively. Fig. 21 (d) is a schematic diagram of how the blast wave applied to the surface of composite material plate. The overpressure of the incident blast wave is 1.33×10^{-3} GPa, and its spectrum range is 0-2 MHz. The analysis time is 200 μs.

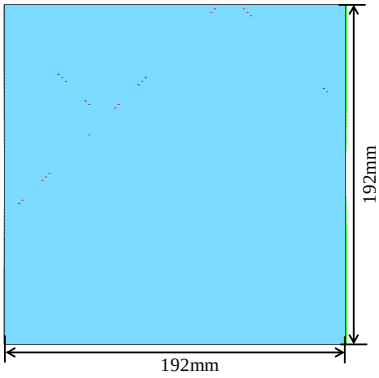

(a) The macro-scale composite material plate

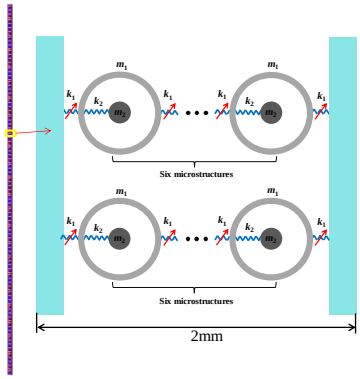

(b) Partial view of the WNLS model

Fig. 20. The macro-scale composite material plate model based on WNLS.

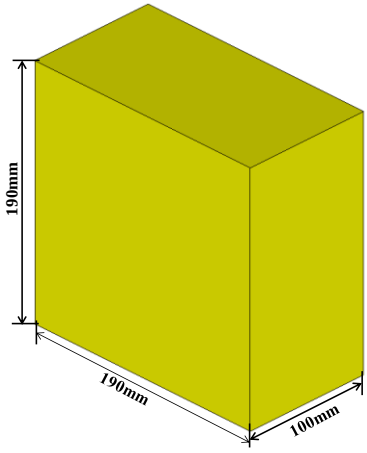

(a) Rubber material

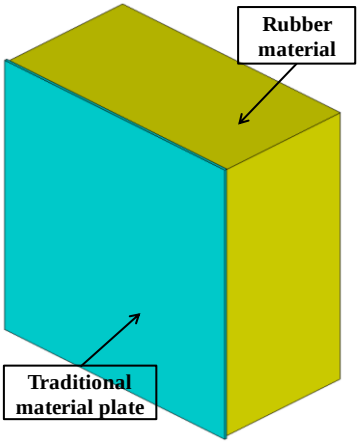

(b) Rubber material with the traditional material plate

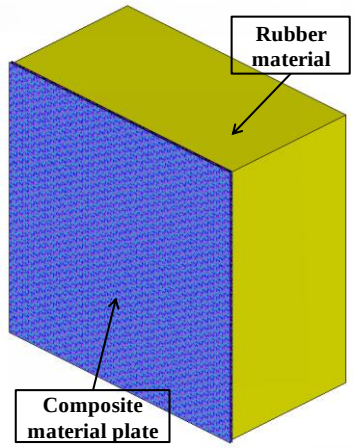

(c) Rubber material with composite material plate

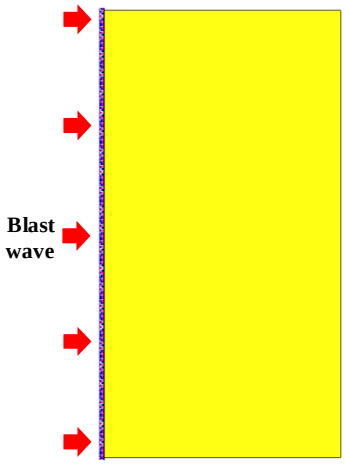

(d) Side view of rubber material with composite material plate under blast wave

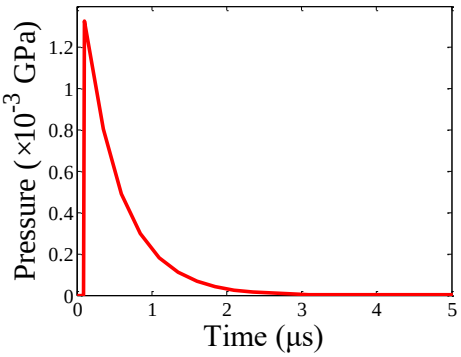

(e) Time-domain curve of blast wave

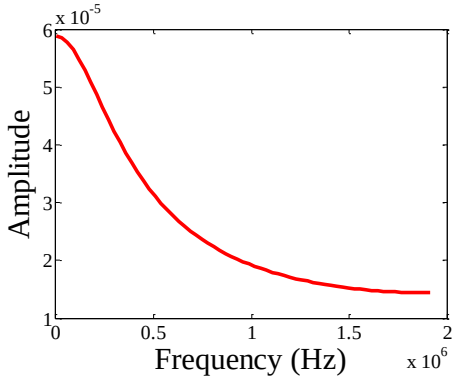

(f) Spectrum curve of blast wave

Fig. 21. Model of rubber material under blast waves.

When the mass of traditional material plate structure is the same as composite material model, the plate thicknesses of resin, aluminum and steel materials are 3.77 mm, 1.45 mm and 0.5 mm, respectively. Table 9 shows the maximum stress of rubber material at different times. The second column of this table is the thickness of the plate structure, and the last column is the maximum structural stress for the entire analysis time. It can be seen that the peak stresses of the rubber material are 18.05×10^{-6} GPa, 24.92×10^{-6} GPa, 36.35×10^{-6} GPa, 19.53×10^{-6} GPa, 16.79×10^{-6} GPa, 16.25×10^{-6} GPa and 15.95 $\times10^{-6}$ GPa when the corresponding time is 5μs, 10μs, 20μs, 50μs, 100μs, 150μs and 200μs. The maximum structural stress for the entire analysis time is 36.35×10^{-6} GPa. Peak stresses of the resin plate model at different times are 7.71×10-6 GPa, 10.44×10^{-6} GPa, 14.99×10^{-6} GPa, 11.43×10^{-6} GPa, 10.67×10^{-6} GPa,

9.90×10^{-6} GPa and 9.39×10^{-6} GPa, and its maximum structural stress is 15.65×10^{-6} GPa. Peak structural stresses of the aluminum plate model at different times are 5.70×10^{-6} GPa, 9.67×10^{-6} GPa, 14.25×10^{-6} GPa, 12.55×10^{-6} GPa, 10.96×10^{-6} GPa, 10.08×10^{-6} GPa and 9.55×10^{-6} GPa, and its maximum value is 15.84×10^{-6} GPa. Peak stresses of the steel plate model are 6.68×10^{-6} GPa, 11.95×10^{-6} GPa, 18.22×10^{-6} GPa, 15.32×10^{-6} GPa, 12.53×10^{-6} GPa, 11.21×10^{-6} GPa and 10.54×10^{-6} GPa, and its maximum value is 19.90×10^{-6} GPa. Peak stresses of the composite material plate model at different times are 3.21×10^{-6} GPa, 5.27×10^{-6} GPa, 7.48×10^{-6} GPa, 5.09×10^{-6} GPa, 4.73×10^{-6} GPa, 4.67×10^{-6} GPa and 4.59×10^{-6} GPa, and its maximum value is 7.48×10^{-6} GPa. Therefore, the peak structural stress of the composite material model is significantly lower than the original, resin, aluminum and steel models. Fig. 22 (a) is the history curve of maximum stress and time of the rubber material corresponding to different models with the same structure mass. It can be seen that the peak stress of all models have a sharp rise at about 0 ~ 25μs, and then gradually decrease with time. In addition, the maximum stress of the rubber material of the composite material model is significantly lower than the other models throughout the whole analysis time.

When the thickness of the traditional material and composite material structures are the same, the masses of the resin, aluminum and steel plate structures are 0.077 kg, 0.199 kg and 0.579 kg, respectively. The analysis results of these models are shown in Fig. 22 (b) and Table 10. The second column of Table 10 is the mass of different plate structures. It can be seen that the peak stresses of the resin plate model are 12.56×10^{-6} GPa, 18.14×10^{-6} GPa, 24.16×10^{-6} GPa, 16.49×10^{-6} GPa, 14.16×10^{-6} GPa, 12.70×10^{-6} GPa and 12.90×10^{-6} GPa when the corresponding time is 5μs, 10μs, 20μs, 50μs, 100μs, 150μs and 200μs. The maximum stress of the whole analysis time is 24.16×10^{-6} GPa. Peak stresses of the aluminum plate model at different times are 4.21×10^{-6} GPa, 7.07×10^{-6} GPa, 11.36×10^{-6} GPa, 11.05×10^{-6} GPa, 9.26×10^{-6} GPa, 8.67×10^{-6} GPa and 8.30×10^{-6} GPa, and the maximum stress is 12.88×10^{-6} GPa. Peak stresses of the steel plate model at different times are 1.62×10^{-6} GPa, 2.86×10^{-6} GPa, 5.61×10-6 GPa, 7.40×10^{-6} GPa, 5.42×10^{-6} GPa, 5.48×10^{-6} GPa and 5.26×10^{-6} GPa,

and its maximum stress is 7.70×10^{-6} GPa. Therefore, peak stress of the composite material model is still the smallest, which is significantly lower than the resin and aluminum models, and slightly lower than the steel model. Meanwhile, structural mass of the composite material structure is significantly lower than that of the aluminum and steel models. From Fig. 22 (b), the peak stress curves of the resin and aluminum models are close, which are significantly higher than the composite material model. The peak stress curve of the steel model is significantly lower than that of the resin and aluminum models, but slightly higher than the composite material model.

The above analysis results show that: (1) the composite material with RSs can effectively mitigate the BWR, (2) with the same structure mass or plate thickness, composite material achieves better attenuation effect compared with traditional material models, (3) composite material model has higher light weight potential than other models.

Table 9. Maximum stress of rubber material with the same plate mass.

	Thickness (mm)	5 (μs)	10 (μs)	20 (μs)	50 (μs)	100 (μs)	150 (μs)	200 (μs)	0-200 (μs)
Pure rubber ($\times10^{-6}$ GPa)	——	18.05	24.92	36.35	19.53	16.79	16.25	15.95	36.35
Resin ($\times10^{-6}$ GPa)	3.77	7.71	10.44	14.99	11.43	10.67	9.90	9.39	15.65
Aluminum ($\times10^{-6}$ GPa)	1.45	5.70	9.67	14.25	12.55	10.96	10.08	9.55	15.84
Steel ($\times10^{-6}$ GPa)	0.50	6.68	11.95	18.22	15.32	12.53	11.21	10.54	19.90
Composite material ($\times10^{-6}$ GPa)	2.00	3.21	5.27	7.48	5.09	4.73	4.67	4.59	7.48

Table 10. Maximum stress of rubber material with the same plate thickness.

	Mass (kg)	5 (μs)	10 (μs)	20 (μs)	50 (μs)	100 (μs)	150 (μs)	200 (μs)	0-200 (μs)
Pure rubber ($\times10^{-6}$ GPa)	——	18.05	24.92	36.35	19.53	16.79	16.25	15.95	36.35
Resin ($\times10^{-6}$ GPa)	0.077	12.56	18.14	24.16	16.49	14.16	12.70	12.90	24.16
Aluminum ($\times10^{-6}$ GPa)	0.199	4.21	7.07	11.36	11.05	9.26	8.67	8.30	12.88
Steel ($\times10^{-6}$ GPa)	0.579	1.62	2.86	5.61	7.40	5.42	5.48	5.26	7.70
Composite material ($\times10^{-6}$ GPa)	0.145	3.21	5.27	7.48	5.09	4.73	4.67	4.59	7.48

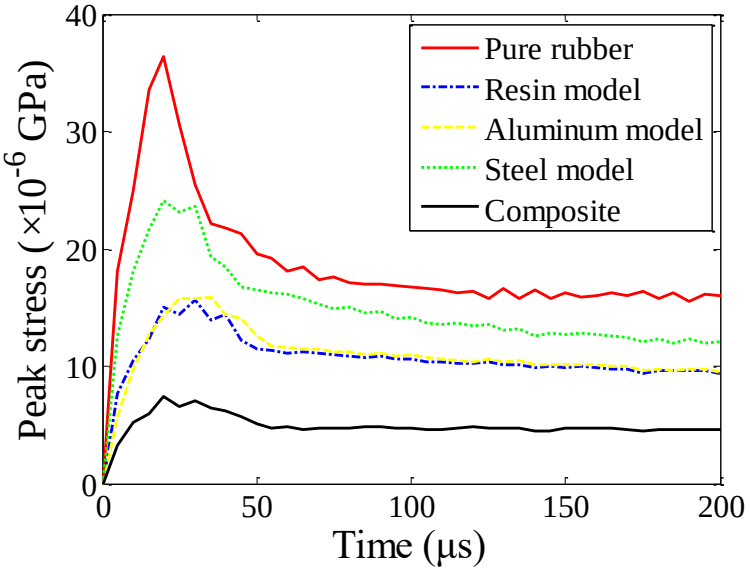

(a) Curves of peak stress and time of different models under the same structure mass

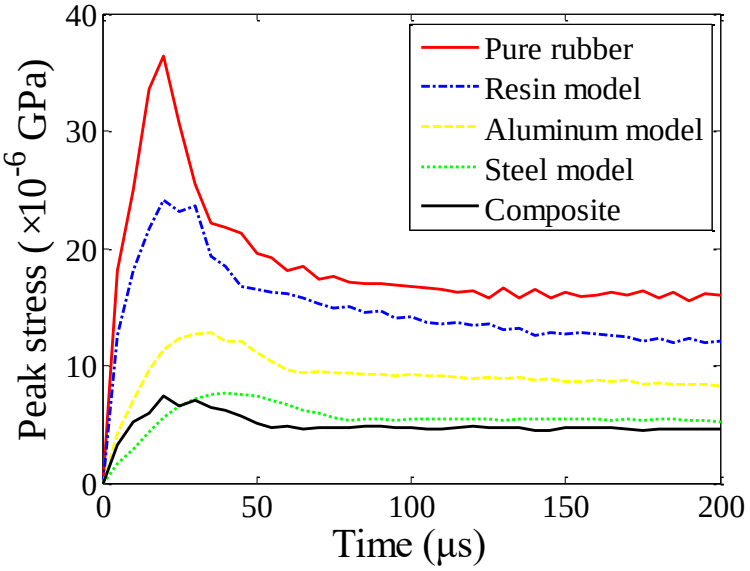

(b) Curves of peak stress and time of different models under the same structure thickness

Fig. 22. Peak stress curves of rubber material.

Figs. 23 and 24 are the stress nephograms of the pure rubber model and the composite material model at different times. From Fig. 23, the structural stress is first created at the four edges of the rubber material and increases over time. At about 20 ms, the amplitude of the stress reaches its maximum value. At about 50 ms, the stress waves are transmitted about 13 mm along the side of the rubber material, and the phenomenon of stress concentration occurs in the central area of the rubber. Over time,

stress waves continue to propagate along the side of the rubber material. At about 100 ms and 150 ms, the stress waves propagate to around 22mm and 32mm, respectively, and the stress concentration mainly occurs at the front of the stress waves. In addition, the stress in the center of the rubber appears wavy. In Fig. 24 (a), the structural stress appears around rubber material first. At approximately 20 ms, the magnitude of the stress reaches its maximum value. After 50 ms, the stress starts to concentrate on the central area of the rubber material. Compared with the pure rubber model, the stress is more evenly distributed in the central area of the composite material model. In short, from Figs. 23 and 24, the stress amplitude of the composite material model is significantly smaller than that of the pure rubber model at each time. Therefore, the composite material model can effectively attenuate the blast wave and alleviate the damage of the rubber material.

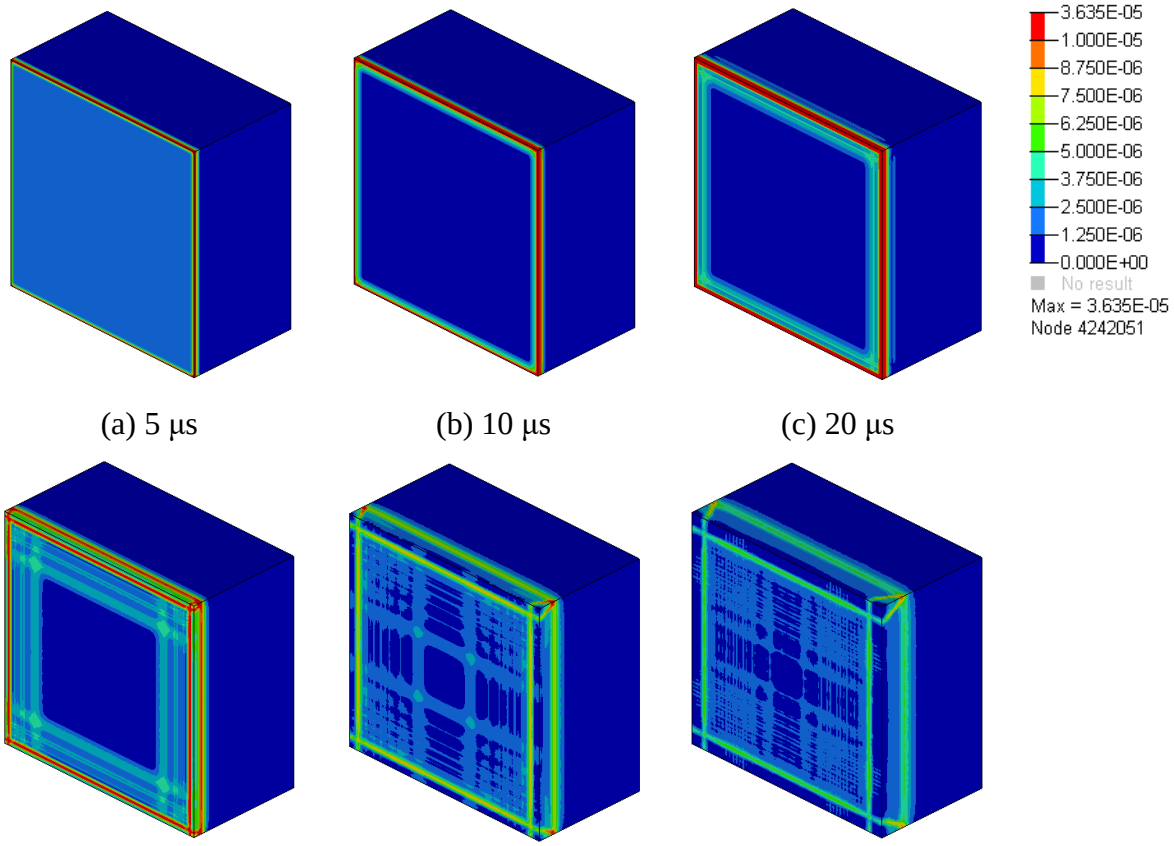

(a) 5 μs (b) 10 μs (c) 20 μs

(d) 50 μs (e) 100 μs (f) 150 μs

Fig. 23. Stress nephograms of the pure rubber material.

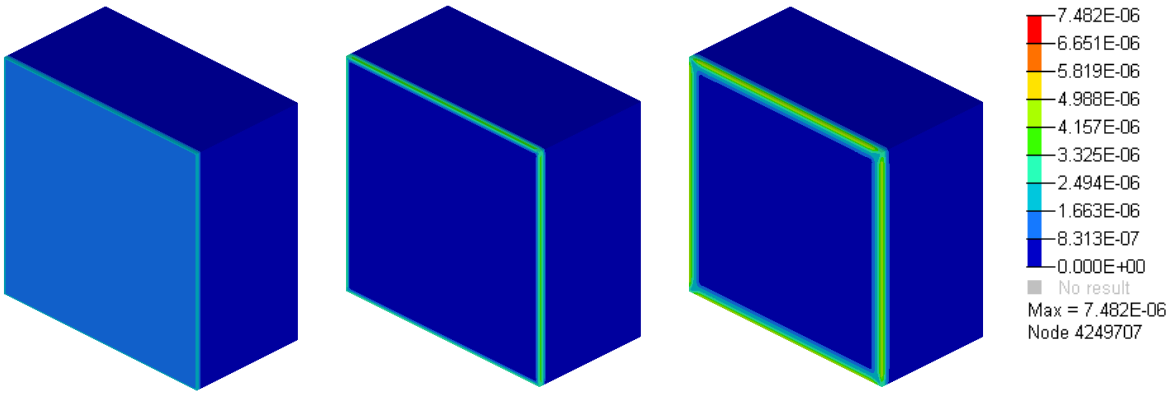

(a) 5 μs (b) 10 μs (c) 20 μs

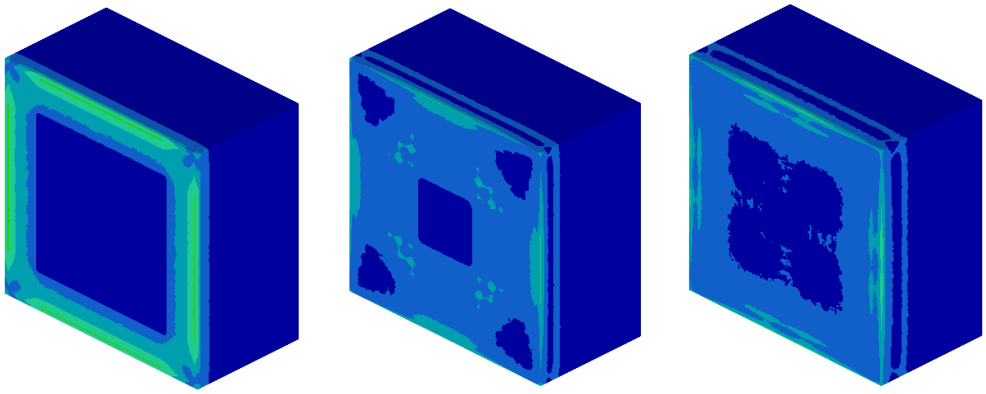

(d) 50 μs (e) 100 μs (f) 150 μs

Fig. 24. Stress nephograms of the rubber material with composite material plate.

5 Description of the experimental scheme

Compared with the process of simulation analyses, we provide a preliminary experimental scheme to verify the attenuation effect of the composite material. Computer-aided design (CAD) technique is applied to construct the three dimensional model of the composite material, and 3D printing technology can be applied for the manufacture of the composite material. A shock tube [39, 40] can be applied to generate and propagate the blast waves.

The experimental process is summarized as follows. (1) The ideal blast wave is obtained by changing the parameters of the shock tube. (2) Impact tests are carried out in five cases. The first case is that the rubber material is impacted directly by the blast wave generated by the shock tube, and the damage of the rubber material is recorded. The second case is to combine the rubber and composite materials, and the composite material plate is placed before the rubber material. The blast wave impacts the composite material directly, and the stress wave generated by the impact will

propagate to the rubber material and cause damage to it. The damage of the rubber material in this case is recorded. The third, fourth and fifth cases are that experiments are performed by replacing the composite material plate in the second case with the steel, aluminum and resin plates, respectively. The results of these three cases are also recorded. (3) The attenuation effect of the composite material is verified by comparing the damage of the rubber material in all cases.

Although this is a preliminary experimental scheme and many details need to be refined, this strategy provides a clear and feasible idea for experimental verification. In addition, the focus of this work is to study the propagation mechanism of stress waves, explore the energy absorption mechanism of RSs, demonstrate the attenuation effect of composite materials and propose the equivalent model of the composite materials with RSs through simulated analyses. Therefore, the authors expect to exhibit the experimental process of this work in detail and share these verification results with the academic community in the subsequent work.

6 Conclusion

In this work, a three-dimensional micro-scale artificial composite materials consist of resonant structures (RSs) and resin matrix are designed to mitigate the blast wave with a very wide frequency range (BWR). Analyses of propagation characteristic of stress waves, energy absorption and material sensitivity are carried out to study the attenuation effect of the composite materials. Computational results show that: (1) RSs can significantly attenuate the blast wave, (2) the better attenuation effect of blast wave requires heavy oscillator and reasonable coating stiffness. An improved RS is presented to further enhance the performance of the composite material. In addition, an equivalent modeling method for constructing the high-precision macro-scale composite material is presented to study blast wave protection. A weakly nonlinear lattice system (WNLS) is applied first to equal the attenuation effect of the composite material, and the spring stiffness parameters is obtained based on the AT (artificial tree) algorithm. Then, a macro-scale composite material plate structure is established based on the WNLS. Finally, the composite

material model is applied to attenuate the BWR and protect the rubber material at the macro-scale. Analysis results indicate that: (1) the composite material model realizes great attenuation effect of the BWR, (2) compared with traditional materials, composite material achieves better attenuation effect and exhibits superior lightweight potential. This work shows the broad application prospect of artificial composite material with RSs and resin matrix in the field of blast protection.

References

1. Eierud C, Nathan DE, Bonavia GH, Ollinger J, Riedy G. **Cortical thinning in military blast compared to non-blast persistent mild traumatic brain injuries**. *NeuroImage: Clinical* 2019; 22:101793.
2. Zander NE, Piehler T, Banton R, Boggs M. **The effect of explosive blast loading on human neuroblastoma cells**. *Analytical Biochemistry* 2016; 504:4-6.
3. Bornstein H, Ryan S, Mouritz AP. **Blast mitigation with fluid Containers: Effect of mitigant type**. *International Journal of Impact Engineering* 2018; 113:106-117.
4. Jin M, Hao Y, Hao H. **Numerical study of fence type blast walls for blast load mitigation**. *International Journal of Impact Engineering* 2019; 131:238-255.
5. Kumar SSP, Ramamurthi K, Patnaik BSV. **Numerical study of a foam-shock trap based blast mitigation strategy**. *Physics of Fluids* 2018; 30(8):086102.
6. Pontalier Q, Loiseau J, Goroshin S, Frost DL. **Experimental investigation of blast mitigation and particle–blast interaction during the explosive dispersal of particles and liquids**. *Shock Waves* 2018; 28(3):489-511.
7. Xiao W, Andrae M, Gebbeken N. **Experimental investigations of shock wave attenuation performance using protective barriers made of woven wire mesh**. *International Journal of Impact Engineering* 2019; 131:209-221.
8. Nesterenko VF. **Shock (Blast) Mitigation by "Soft" Condensed Matter**. *MRS Proceedings* 2002; 759:MM4.3.
9. Christou GA, Young LR, Goel R, Vechart AP, Jérusalem A. **Shock attenuation of PMMA sandwich panels filled with soda-lime glass beads: A fluid-structure interaction continuum model simulation**. *International Journal of Impact Engineering* 2012; 47:48-59.
10. Wadley HNG, Dharmasena KP, He MY, McMeeking RM, Evans AG, Bui-Thanh T, et al. **An active concept for limiting injuries caused by air blasts**. *International Journal of Impact Engineering* 2010; 37(3):317-323.
11. Su Z, Peng W, Zhang Z, Gogos G, Skaggs R, Cheeseman B. **Numerical simulation of a novel blast wave mitigation device**. *International Journal of Impact Engineering* 2008; 35(5):336-346.
12. Vivek P, Sitharam TG. **Shock wave attenuation by geotextile encapsulated sand barrier systems**. *Geotextiles and Geomembranes* 2017; 45(3):149-160.

13. Igra D, Igra O. **Shock wave mitigation by different combination of plate barriers; a numerical investigation**. *European Journal of Mechanics - B/Fluids* 2016; 59:115-123.
14. Li QQ, He ZC, Li E, Cheng AG. **Design of a multi-resonator metamaterial for mitigating impact force**. *Journal of Applied Physics* 2019; 125(3):035104.
15. Tan KT, Huang HH, Sun CT. **Blast-wave impact mitigation using negative effective mass density concept of elastic metamaterials**. *International Journal of Impact Engineering* 2014; 64:20-29.
16. Alamri S, Li B, Tan KT. **Dynamic load mitigation using dissipative elastic metamaterials with multiple Maxwell-type oscillators**. *Journal of Applied Physics* 2018; 123(9):095111.
17. Li QQ, He ZC, Li E, Cheng AG. **Design and optimization of three-resonator locally resonant metamaterial for impact force mitigation**. *Smart Materials and Structures* 2018; 27(9):095015.
18. Li X, Chen Y, Hu G, Huang G. **A self-adaptive metamaterial beam with digitally controlled resonators for subwavelength broadband flexural wave attenuation**. *Smart Materials and Structures* 2018; 27(4):045015.
19. Nguyen H, Zhu R, Chen JK, Tracy SL, Huang GL. **Analytical coupled modeling of a magneto-based acoustic metamaterial harvester**. *Smart Materials and Structures* 2018; 27(5):055010.
20. Xu J, Li S, Tang J. **Customized shaping of vibration modes by acoustic metamaterial synthesis**. *Smart Materials and Structures* 2018; 27(4):045001.
21. Zhang X, Zhang H, Chen Z, Wang G. **Simultaneous realization of large sound insulation and efficient energy harvesting with acoustic metamaterial**. *Smart Materials and Structures* 2018; 27(10):105018.
22. Wang C, Liu Z, Gao L, Xu D, Zhuang Z. **Analytical and numerical modeling on resonant response of particles in polymer matrix under blast wave**. *Computational Materials Science* 2017; 140:70-81.
23. Mitchell SJ, Pandolfi A, Ortiz M. **Metaconcrete: designed aggregates to enhance dynamic performance**. *Journal of the Mechanics and Physics of Solids* 2014; 65:69-81.
24. Mitchell SJ, Pandolfi A, Ortiz M. **Investigation of elastic wave transmission in a metaconcrete slab**. *Mechanics of Materials* 2015; 91:295-303.
25. Li QQ, He ZC, Li E, Cheng AG. **Improved impact responses of a honeycomb sandwich panel structure with internal resonators**. *Engineering Optimization* 2019:1-22.
26. Li QQ, He ZC, Li E. **Dissipative multi-resonator acoustic metamaterials for impact force mitigation and collision energy absorption**. *Acta Mechanica* 2019; 230(8):2905-2935.
27. Dong J, Jia C, Wang M, Fang X, Wei H, Xie H, et al. **Improved mechanical properties of carbon fiber-reinforced epoxy composites by growing carbon black on carbon fiber surface**. *Composites Science and Technology* 2017; 149:75-80.
28. Ma Q, Gu Y, Li M, Wang S, Zhang Z. **Effects of surface treating methods of high-strength carbon fibers on interfacial properties of epoxy resin matrix**

composite. *Applied Surface Science* 2016; 379:199-205.
29. Das S. **Mechanical properties of waste paper/jute fabric reinforced polyester resin matrix hybrid composites**. *Carbohydrate Polymers* 2017; 172:60-67.
30. Krishnamoorthy K, Pazhamalai MP, Lim JH, Choi KH, Kim S-J. **Mechanochemical Reinforcement of Graphene Sheets into Alkyd Resin Matrix for the Development of Electrically Conductive Paints**. *ChemNanoMat* 2018; 4(6):568-574.
31. Fang X, Wen J, Yin J, Yu D. **Wave propagation in nonlinear metamaterial multi-atomic chains based on homotopy method**. *AIP Advances* 2016; 6(12):121706.
32. Narisetti RK, Leamy MJ, Ruzzene M. **A Perturbation Approach for Predicting Wave Propagation in One-Dimensional Nonlinear Periodic Structures**. *Journal of Vibration and Acoustics* 2010; 132(3):031001.
33. Zhou WJ, Li XP, Wang YS, Chen WQ, Huang GL. **Spectro-spatial analysis of wave packet propagation in nonlinear acoustic metamaterials**. *Journal of Sound and Vibration* 2018; 413:250-269.
34. Yao S, Zhou X, Hu G. **Experimental study on negative effective mass in a 1D mass–spring system**. *New Journal of Physics* 2008; 10(4):043020.
35. Narisetti RK, Leamy MJ, Ruzzene M. **A Perturbation Approach for Predicting Wave Propagation in One-Dimensional Nonlinear Periodic Structures**. *Journal of Vibration and Acoustics* 2010; 132(3).
36. Luo J, Liu Q, Yang Y, Li X, Chen M-r, Cao W. **An artificial bee colony algorithm for multi-objective optimisation**. *Applied Soft Computing* 2017; 50:235-251.
37. Li QQ, Song K, He ZC, Li E, Cheng AG, Chen T. **The artificial tree (AT) algorithm**. *Engineering Applications of Artificial Intelligence* 2017; 65:99-110.
38. Xu H, Zhang L, Li Q. **A novel inverse procedure for load identification based on improved artificial tree algorithm**. *Engineering with Computers* 2019.
39. Thakur R, Jagadeesh G. **Experimental Analysis of Shock Standoff Distance in Hypersonic Flows over Spherical Bodies**. In: *30th International Symposium on Shock Waves 1*: Springer; 2017. pp. 167-171.
40. Aune V, Fagerholt E, Langseth M, Børvik T. **A shock tube facility to generate blast loading on structures**. *International Journal of Protective Structures* 2016; 7(3):340-366.